machines

MDPI

Article

Closed-Loop Wheelbase-Preview Model Predictive Control for Active Suspension Using Reconstructed Road Information

Seonho Jeong [1] and Yonghwan Jeong [2,*]

[1] Department of Automotive Engineering, Seoul National University of Science and Technology, Seoul 01811, Republic of Korea; jeong@seoultech.ac.kr
[2] School of Mechanical Systems Engineering, Seoul National University of Science and Technology, Seoul 01811, Republic of Korea
* Correspondence: yh.jeong@seoultech.ac.kr; Tel.: +82-2-970-6322

Abstract

This study presents a closed-loop wheelbase-preview model predictive control (MPC) method for vehicle pitch-attitude regulation during localized bump traversal without a forward-looking road sensor. Road information reconstructed from front unsprung-mass acceleration supports front-axle compensation and causal rear-axle preview. An existing linear–quadratic static output feedback (LQSOF) controller supplies the baseline force, while MPC optimizes an additional rear command using predictions of future feedback action and actuator dynamics. CarSim–MATLAB/Simulink co-simulations evaluate performance at 20, 30, and 40 km/h. Relative to LQSOF, the complete configuration reduces the pitch-angle RMS by 9.5–17.5% and the pitch-rate RMS by 18.9–24.3%, without uniform improvement in vertical acceleration. Relative to front compensation alone, rear MPC further reduces the pitch-angle RMS by 16.0% and 11.8% at 20 and 30 km/h, but this benefit is not maintained at 40 km/h. A proportional rear-gain sweep identifies condition-dependent trade-offs between pitch regulation, vertical response, and actuator demand. Controlled ablation and sensitivity analyses characterize the prediction-model components and disturbance dependence. Unsuccessful constrained optimization at 50 and 60 km/h limits the current implementation; no incremental high-speed MPC benefit over LQSOF is established.

Keywords: active suspension; model predictive control; wheelbase preview; road reconstruction; body attitude control; vehicle dynamics

1. Introduction

Vehicle suspension systems must simultaneously attenuate road-induced vibration, maintain tire–road contact, limit suspension travel, and regulate body attitude. Recent developments in electrified and intelligent vehicles have renewed interest in fully active suspension systems because faster chassis actuators and increasingly integrated sensing and control architectures provide greater opportunities for active ride control [1]. Among the available control approaches, preview suspension control is particularly attractive because it can initiate suspension action before a road disturbance reaches the controlled axle, thereby providing a degree of anticipation that is unavailable to purely reactive feedback control [2].

Recent studies have increasingly combined road-preview information with model-based and optimization-based suspension control. A regionless explicit MPC framework was developed to incorporate road-preview information while reducing the online computational burden associated with conventional MPC [3]. An incremental MPC strategy was subsequently proposed using road-preview information estimated from a preceding vehicle,

Check for updates

Academic Editors: Zheng Chen and Renkai Ding

Received: 28 September 2026
Revised: 27 October 2026
Accepted: 12 November 2026
Published: 18 November 2026

Copyright: © 2026 by the authors. Licensee MDPI, Basel, Switzerland. This article is an open access article distributed under the terms and conditions of the Creative Commons Attribution (CC BY) license.

demonstrating the feasibility of externally acquired preview information for active suspension control [4]. Preview MPC was also combined with radial basis function networks for active suspension control [5], while road-preview control based on measured road-profile information was investigated to improve vehicle ride response [6]. An adaptive bioinspired preview suspension controller was further integrated with constrained longitudinal-velocity planning for autonomous vehicles [7]. For semi-active suspension systems, preview-based MPC was developed with explicit compensation for the shift delay between the preview information and the suspension response [8].

More recent studies have extended preview suspension control toward speed-dependent operation, integrated vehicle control, learning-based prediction, and robustness to preview uncertainty. A speed-dependent active-suspension MPC was formulated to account for variations in the available road-preview interval with vehicle velocity [9]. Preview active-suspension control was also integrated with longitudinal-velocity planning to improve ride comfort through coordinated suspension and speed control [10]. A learning-enhanced preview MPC framework incorporating Gaussian-process modeling was proposed to improve prediction and active-suspension control [11]. Road-preview MPC was also applied to a semi-active suspension equipped with a magnetorheological damper, extending preview optimization to constrained semi-active actuation [12]. Coupled control of preview active suspension and longitudinal vehicle dynamics was investigated for autonomous vehicle applications [13], while a disturbance-resilient MPC framework was developed to explicitly address errors in perceived road-preview information [14]. Preview control using a virtual-disturbance formulation was also investigated for active suspension systems [15]. These studies indicate that the effectiveness of preview suspension control depends not only on the availability of road information but also on how preview timing, vehicle dynamics, actuator characteristics, and sensing uncertainty are incorporated into the controller.

A central practical issue is the acquisition of reliable road-preview information. Forward-looking LiDAR and camera systems can directly estimate road geometry, and recent work has demonstrated vehicle-level LiDAR-based road-height estimation and bump detection for preview suspension applications [16]. However, external perception increases sensing and processing requirements and can be affected by installation geometry, occlusion, noise, and environmental conditions. For this reason, response-based road estimation remains attractive when suspension or wheel-response signals are already available. Recent approaches have estimated road profiles from unsprung-mass acceleration [17], jointly estimated vehicle states and unknown road inputs [18], used road identification to switch suspension-control modes [19,20], formulated generalized observer-based road estimators [21], and investigated collaborative road-profile estimation for connected vehicles [22]. These methods indicate that useful road information can be recovered from vehicle-response signals without requiring direct geometric measurement of the road surface.

For a two-axle vehicle, front-wheel information can provide a natural source of rear-axle preview. Once the front wheel encounters a disturbance, the same spatial road feature reaches the rear wheel after the wheelbase travel time. A wheelbase-preview control method incorporating a disturbance-decoupled observer was developed to improve vehicle ride comfort using front-axle information for rear-suspension control [23]. Robust static output feedback wheelbase-preview control was subsequently investigated for uncertain active suspension systems while considering time delay and finite-frequency performance [24]. A multi-objective frequency-domain static output feedback approach was also proposed for delayed active suspension systems using wheelbase-preview information [25]. More recently, road elevation recognition was combined with rear-suspension wheelbase preview to improve vehicle posture control on uneven road surfaces [26]. An augmented-

Kalman-filter-based road estimate was further incorporated into a wheelbase-preview predictive controller, in which the estimated front-road profile was shifted according to the wheelbase travel time and used within an MPC formulation for rear-suspension control [27]. A time-varying delay control method based on an equivalent-frequency-band formulation was also proposed to address varying preview delays in suspension control [28]. These studies demonstrate the potential of wheelbase preview for utilizing road information already encountered by the front axle, thereby reducing dependence on forward-looking road sensors.

Beyond preview-oriented control, recent active-suspension studies have addressed broader vehicle and occupant dynamics. In [29], a half-car suspension model was integrated with seat and human biodynamic models, and Gray Wolf Optimization was employed to tune an LQR controller, with performance evaluated under stochastic road excitation. Another study [30] investigated an enhanced static output feedback H∞ control framework for a half-vehicle suspension incorporating vertical and roll dynamics, with particular emphasis on vibration attenuation and time-delay robustness. These studies highlight the importance of occupant-related vibration responses, multi-axis body dynamics, and implementation robustness in active-suspension design. In contrast, the present study focuses on longitudinal heave–pitch dynamics and the closed-loop integration of reconstructed-road wheelbase-preview control with an existing LQSOF controller and finite-bandwidth actuators.

Although preview control enables anticipatory suspension action, reliable road-profile information cannot always be obtained under all driving conditions, particularly without forward-looking sensors. In the present sensor configuration, road information becomes available only after the front wheel encounters a disturbance, and its reconstruction accuracy may vary with road conditions. Therefore, the baseline LQSOF controller is retained to provide the primary feedback response to road disturbances, independently of the availability of reconstructed road information. The proposed additive MPC is introduced to further improve suspension performance by exploiting causally available road information for rear-axle wheelbase-preview control. This modular arrangement maintains the existing feedback-control structure while extending its functionality through preview control, consistent with established modular feedback-preview approaches [31]. Since the additional preview force affects subsequent feedback actions and is delivered through finite-bandwidth actuators, these interactions are explicitly incorporated into the MPC prediction model.

Road-estimation-based wheelbase-preview MPC has already been investigated in [27], where an augmented Kalman filter estimates vehicle states and the front-road profile, and a shift register provides the preview information for MPC-based suspension-force optimization. In contrast, the present study focuses on integrating preview control with an existing LQSOF-controlled suspension. Rather than replacing the baseline controller, the MPC optimizes only an additional rear-preview force while explicitly predicting the future LQSOF action and actuator-force dynamics. This formulation accounts for the interaction between feedback and preview commands and imposes the physical actuator constraint on their combined command. The methodological contribution therefore lies in the closed-loop formulation of the additive preview layer rather than in road-estimation-based wheelbase preview or MPC itself.

The objective of this study is to improve vehicle pitch-attitude regulation during localized bump traversal using reconstructed-road wheelbase-preview information without a forward-looking road sensor. LQSOF provides the baseline suspension response, while reconstructed front-road information is used for front-axle compensation and causal rear-axle preview. The proposed MPC optimizes an additive rear command while accounting for future baseline feedback action and finite actuator-response dynamics.

The pitch angle and pitch rate are the principal response indices used to assess the proposed framework, with vertical acceleration and actuator demand evaluated as accompanying trade-offs. The optimization retains coupled heave–pitch performance terms and is not restricted to pitch motion alone. Front-compensation-only and proportional rear-gain comparisons distinguish the incremental rear-MPC contribution from the performance of the complete control configuration. The principal evaluation covers the investigated 20–40 km/h conditions, while unsuccessful higher-speed operation is reported as a limitation of the current implementation.

The main contributions of this study are summarized as follows:

1. The established feedback-embedded closed-loop MPC framework is adapted to an existing LQSOF-controlled active suspension by incorporating predictions of future baseline feedback action and first-order actuator-force dynamics into the rear-preview optimization.
2. A causal wheelbase-preview MPC framework is constructed using reconstructed front-road information without requiring an additional forward-looking road sensor.
3. An additive rear-preview MPC formulation is introduced in which only the additional rear-axle force is optimized, while the physical actuator constraint is imposed on the combined feedback and preview commands.
4. The prediction-model components are assessed through controlled ablation, and the incremental contribution of rear MPC is examined using a front-compensation-only reference. Proportional rear-gain sensitivity and disturbance-related evaluations characterize the performance trade-offs and operating limitations of the proposed framework.

The remainder of this paper is organized as follows: Section 2 presents the vehicle model, actuator dynamics, and wheelbase-preview framework. Section 3 introduces the proposed closed-loop wheelbase-preview MPC formulation. Section 4 presents the simulation environment, comparative suspension-performance results, and additional ablation, sensitivity, and computational analyses. Finally, Section 5 summarizes the main findings and conclusions.

2. Vehicle Model and Control Framework

A control-oriented pitch-plane half-car model is adopted to formulate the proposed wheelbase-preview controller. The present study focuses on road disturbances, such as a bump, that are applied symmetrically to the left and right wheels. Under this condition, the dominant vehicle motions are the sprung-mass heave and pitch responses together with the vertical motions of the front and rear unsprung masses. Accordingly, roll dynamics are neglected, and the left and right wheels at each axle are represented by an equivalent axle-level model.

The half-car model is used to describe the vehicle, baseline feedback controller, and active-actuator dynamics required for the wheelbase-preview formulation. This model subsequently provides the basis for the closed-loop predictive model developed in Section 3.

2.1. Vehicle and Actuator Model

The control-oriented pitch-plane half-car model used in this study is shown in Figure 1. Let z_c and θ denote the vertical displacement and pitch angle of the sprung mass, respectively, and let $z_{u,f}$ and $z_{u,r}$ denote the equivalent front- and rear-axle unsprung-mass displacements. The vertical positions of the sprung mass at the front and rear suspension attachment points are expressed, under the small-pitch-angle assumption, as

$$\begin{aligned} z_{s,f} &= z_c - l_f\theta \\ z_{s,r} &= z_c + l_r\theta \end{aligned} \tag{1}$$

where l_f and l_r are the longitudinal distances from the vehicle center of gravity to the front and rear axles, respectively.

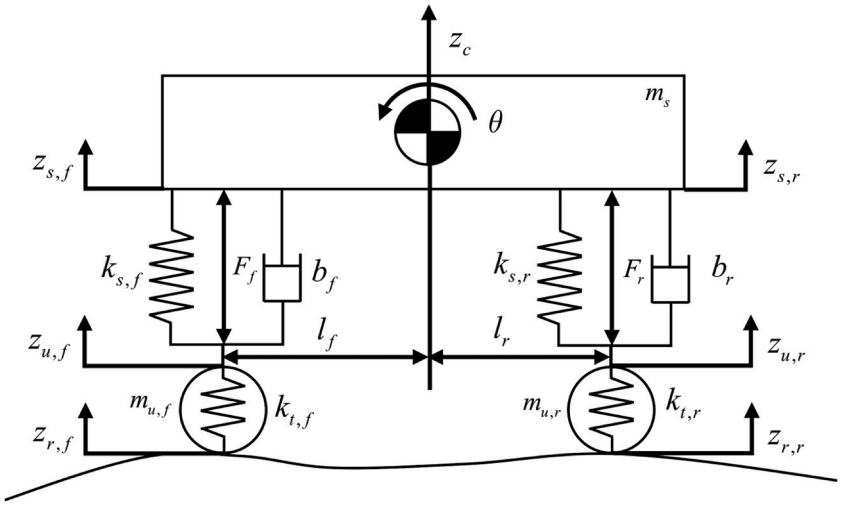


Figure 1. Control-oriented pitch-plane half-car model used for the baseline controller and closed-loop MPC formulation.

The equivalent suspension forces at the two axles are expressed as

$$\begin{aligned} f_f &= -k_{s,f}\left(z_{s,f} - z_{u,f}\right) - b_f\left(\dot{z}_{s,f} - \dot{z}_{u,f}\right) + F_f \\ f_r &= -k_{s,r}\left(z_{s,r} - z_{u,r}\right) - b_r\left(\dot{z}_{s,r} - \dot{z}_{u,r}\right) + F_r \end{aligned} \tag{2}$$

where $k_{s,f}$ and $k_{s,r}$ are the equivalent axle-level suspension stiffnesses, b_f and b_r are the corresponding damping coefficients, and F_f and F_r denote the actual forces generated by the front and rear active actuators.

The sprung-mass heave and pitch dynamics are then given by

$$\begin{aligned} m_s\ddot{z}_c &= f_f + f_r \\ I_y\ddot{\theta} &= -l_f f_f + l_r f_r \end{aligned} \tag{3}$$

where m_s and I_y denote the sprung mass and its pitch moment of inertia, respectively. The vertical dynamics of the front and rear unsprung masses are written as

$$\begin{aligned} m_{u,f}\ddot{z}_{u,f} &= -f_f - k_{t,f}\left(z_{u,f} - z_{r,f}\right) \\ m_{u,r}\ddot{z}_{u,r} &= -f_r - k_{t,r}\left(z_{u,r} - z_{r,r}\right) \end{aligned} \tag{4}$$

where $m_{u,f}$ and $m_{u,r}$ are the equivalent unsprung masses, $k_{t,f}$ and $k_{t,r}$ are the tire vertical stiffnesses, and $z_{r,f}$ and $z_{r,r}$ represent the front and rear road inputs.

For compact controller formulation, the generalized coordinates, actuator forces, and road disturbances are defined as

$$\begin{aligned} \mathbf{q} &= \begin{bmatrix} z_c & \theta & z_{u,f} & z_{u,r} \end{bmatrix}^T \\ \mathbf{F}_a &= \begin{bmatrix} F_f & F_r \end{bmatrix}^T, \quad \mathbf{w} = \begin{bmatrix} z_{r,f} & z_{r,r} \end{bmatrix}^T \end{aligned} \tag{5}$$

The equations of motion can consequently be represented in the second-order form

$$\mathbf{M}\ddot{\mathbf{q}} + \mathbf{C}\dot{\mathbf{q}} + \mathbf{K}\mathbf{q} = \mathbf{G}_u\mathbf{F}_a + \mathbf{G}_w\mathbf{w} \tag{6}$$

with

$$\mathbf{M} = \mathrm{diag}\left(m_s,\ I_y,\ m_{u,f},\ m_{u,r}\right)$$
$$\mathbf{G}_u = \begin{bmatrix} 1 & 1 \\ -l_f & l_r \\ -1 & 0 \\ 0 & -1 \end{bmatrix},\ \mathbf{G}_w = \begin{bmatrix} 0 & 0 \\ 0 & 0 \\ k_{t,f} & 0 \\ 0 & k_{t,r} \end{bmatrix},\ \mathbf{C} = \begin{bmatrix} b_f + b_r & -b_f l_f + b_r l_r & -b_f & -b_r \\ -b_f l_f + b_r l_r & b_f l_f^2 + b_r l_r^2 & b_f l_f & -b_r l_r \\ -b_f & b_f l_f & b_f & 0 \\ -b_r & -b_r l_r & 0 & b_r \end{bmatrix} \tag{7}$$
$$\mathbf{K} = \begin{bmatrix} k_{s,f} + k_{s,r} & -k_{s,f} l_f + k_{s,r} l_r & -k_{s,f} & -k_{s,r} \\ -k_{s,f} l_f + k_{s,r} l_r & k_{s,f} l_f^2 + k_{s,r} l_r^2 & k_{s,f} l_f & -k_{s,r} l_r \\ -k_{s,f} & k_{s,f} l_f & k_{s,f} + k_{t,f} & 0 \\ -k_{s,r} & -k_{s,r} l_r & 0 & k_{s,r} + k_{t,r} \end{bmatrix}$$

The matrices **M**, **C**, and **K** are determined from the vehicle parameters and suspension geometry, while $\mathbf{G}_u$ and $\mathbf{G}_w$ define the distributions of the actuator forces and road inputs, respectively.

The corresponding vehicle state vector is defined as

$$\mathbf{x}_v = \begin{bmatrix} \mathbf{q}^T & \dot{\mathbf{q}}^T \end{bmatrix}^T \tag{8}$$

and the continuous-time state-space model becomes

$$\begin{aligned} \dot{\mathbf{x}}_v &= \mathbf{A}_v \mathbf{x}_v + \mathbf{B}_F \mathbf{F}_a + \mathbf{B}_w \mathbf{w} \\ \mathbf{A}_v &= \begin{bmatrix} \mathbf{0}_{4\times4} & \mathbf{I}_4 \\ -\mathbf{M}^{-1}\mathbf{K} & -\mathbf{M}^{-1}\mathbf{C} \end{bmatrix} \\ \mathbf{B}_F &= \begin{bmatrix} \mathbf{0}_{4\times2} \\ \mathbf{M}^{-1}\mathbf{G}_u \end{bmatrix},\quad \mathbf{B}_w = \begin{bmatrix} \mathbf{0}_{4\times2} \\ \mathbf{M}^{-1}\mathbf{G}_w \end{bmatrix} \end{aligned} \tag{9}$$

The resulting axle-level state-space model is used for controller formulation under the laterally symmetric road condition considered in this study. The actuator dynamics are further included to account for the finite force response in the predictive controller.

Each active actuator is modeled using a first-order force response,

$$\begin{aligned} T_a \dot{\mathbf{F}}_a + \mathbf{F}_a &= \mathbf{u}_{cmd} \\ \dot{\mathbf{F}}_a &= -\tfrac{1}{T_a}\mathbf{F}_a + \tfrac{1}{T_a}\mathbf{u}_{cmd} \end{aligned} \tag{10}$$

where T_a is the actuator time constant, and $\mathbf{u}_{cmd}$ denotes the commanded front- and rear-axle active-force vector. The first-order actuator model is adopted to represent the dominant command-to-force dynamics while maintaining a computationally tractable prediction model. The nominal time constant is set to $T_a = 0.0199$ s, corresponding to an assumed first-order force-response bandwidth of approximately 8 Hz. Each actuator is represented by a first-order command-to-force model implemented in Simulink, and the resulting actuator force is applied to the CarSim full-vehicle model. The same nominal actuator dynamics are incorporated into the MPC prediction model. The selected bandwidth represents a prescribed simulation parameter rather than an experimentally identified characteristic of a specific physical actuator. The sensitivity to deviations from this nominal response is further investigated in Section 4.4.2. The commanded axle-level force is constrained as

$$\left|u_{cmd,i}\right| \le u_{max},\quad i \in \{f, r\} \tag{11}$$

The actuator force is retained as a dynamic state in the proposed prediction model, allowing the MPC to account for the difference between the commanded force and the force delivered to the suspension.

2.2. Baseline Control and Wheelbase-Preview Information

The proposed controller is constructed as an additional preview layer on top of the baseline active-suspension controller. A LQSOF controller is employed to provide the primary feedback control force, while the reconstructed road information is used to generate additional front- and rear-axle control actions. The feedback vector contains the pitch rate and the vertical velocity information of the sprung and unsprung masses, avoiding the need for direct feedback of absolute vertical displacement.

For the pitch-plane model, the feedback output is defined as

$$\begin{aligned} \mathbf{y} &= \begin{bmatrix} \dot{\theta} & \dot{z}_{s,f} & \dot{z}_{s,r} & \dot{z}_{u,f} & \dot{z}_{u,r} \end{bmatrix}^T \\ \mathbf{y} &= \mathbf{C}_y \mathbf{x}_v \end{aligned} \tag{12}$$

with

$$\begin{aligned} \mathbf{C}_y &= \begin{bmatrix} \mathbf{0}_{5\times4} & \mathbf{C}_v \end{bmatrix} \\ \mathbf{C}_v &= \begin{bmatrix} 0 & 1 & 0 & 0 \\ 1 & -l_f & 0 & 0 \\ 1 & l_r & 0 & 0 \\ 0 & 0 & 1 & 0 \\ 0 & 0 & 0 & 1 \end{bmatrix} \end{aligned} \tag{13}$$

The baseline active-suspension command is generated using the static output feedback law.

$$\mathbf{u}_{LQ} = -\mathbf{K}_{SOF}\mathbf{y} = -\mathbf{K}_{SOF}\mathbf{C}_y\mathbf{x}_v \tag{14}$$

The total actuator command in the present architecture is written as

$$\begin{aligned} \mathbf{u}_{cmd} &= \mathbf{u}_{LQ} + \mathbf{u}_{add} \\ \mathbf{u}_{add} &= \begin{bmatrix} u_{c,f} \\ u_{p,r} \end{bmatrix} \end{aligned} \tag{15}$$

where $\mathbf{u}_{LQ}$ denotes the baseline front- and rear-axle commands, $u_{c,f}$ denotes the front-axle road-based compensation generated using the reconstructed road information, and $u_{p,r}$ denotes the rear-axle preview force generated by the proposed MPC. Because the reconstructed front-road signal becomes available only after front-wheel contact, $u_{c,f}$ is a post-contact compensation term rather than a temporal preview input. By contrast, the rear control action can exploit the longitudinal separation between the two axles and is therefore a genuine wheelbase-preview action.

The front-road profile is reconstructed from the front unsprung-mass acceleration using an inverse road-to-wheel transfer-function approach:

$$\hat{z}_{r,f}(z) = H_{HP}(z)H_{rw}^{-1}(z)\ddot{z}_{u,f}(z) \tag{16}$$

The road-to-wheel transfer function was empirically identified using the front-road elevation and corresponding unsprung-mass vertical acceleration obtained from CarSim simulations. The identification dataset consisted of repeated bump excitations under smooth and ISO Class A/B road conditions at 30 km/h. A discrete transfer function with numerator and denominator orders of 8 and 7, respectively, was identified using the MATLAB System Identification Toolbox at a sampling interval of 1 ms.

The identified transfer function provides a linear approximation of the road-to-wheel relationship within the investigated excitation conditions. Its purpose is to support the reconstruction of road information rather than to reproduce the complete physical dynamics of the vehicle.

The front-road profile was reconstructed using the inverse transfer function followed by a second-order high-pass filter (HPF) with a natural frequency of 0.1 Hz and a damping

ratio of 0.45. The HPF was discretized using the zero-order-hold method at 1 ms to suppress low-frequency reconstruction drift. The road information supplied to the controller was obtained from this complete filtered reconstruction process.

For reproducibility, the inverse road-to-wheel transfer function, $H_{wr}(z) = {H_{rw}}^{-1}(z)$, was implemented using numerator coefficients $\beta = [-0.018627, 0.019899, 0.034436, -0.005550, -0.078832, 0.017274, 0.062977, -0.031575]$ and denominator coefficients $\alpha = [1.000000, -0.022279, -1.372174, -1.292530, 0.391529, 1.389160, 0.597104, -0.074352, -0.616458]$. The coefficients are arranged in ascending powers of z^{-1} and were retained unchanged throughout the road-reconstruction and controller evaluations.

The stability of the road-reconstruction process was examined using the complete filtered reconstruction transfer function rather than the isolated inverse-model factor. At the reported coefficient precision, the inverse-model denominator contains a pole at $z = 1$, which is analytically canceled by the corresponding zero of the discretized HPF. After cancellation, all poles of the reduced reconstruction transfer function lie strictly inside the unit circle, with a maximum magnitude of approximately 0.999999604. This establishes nominal input–output stability of the reduced reconstruction mapping without modifying the original transfer-function coefficients.

The pole near $z = -1$ remains weakly damped, and the HPF does not eliminate its potential sensitivity to high-frequency measurement noise. In addition, analytical pole-zero cancellation does not necessarily guarantee the asymptotic stability of all internal states in a separate-block implementation. Therefore, the reconstruction accuracy and measurement-noise sensitivity are evaluated separately in Section 4.4.3.

The reciprocal road-to-wheel approximation also contains poles outside the unit circle. These poles are not interpreted as physical instabilities of the simulated vehicle. Their occurrence may reflect limitations associated with the finite identification dataset and the selected linear transfer-function approximation. Consequently, the identified forward model is not treated as an independently validated physical representation of the vehicle dynamics. The full-vehicle responses are generated by CarSim, while the identified transfer function is used for road reconstruction within the investigated conditions.

The reconstructed road information is used to generate an additional front-axle compensation force. A proportional compensation law is employed as

$$u_{c,f}(k) = K_{c,f}\hat{z}_{r,f}(k) \tag{17}$$

where $K_{c,f}$ denotes the front-axle road-compensation gain, including the sign required by the actuator-force convention. In contrast, the same reconstructed road information can be utilized as preview information for the rear suspension owing to the longitudinal separation between the front and rear axles.

For straight-line motion at longitudinal velocity v_x, the time required for a road disturbance to travel from the front axle to the rear axle is

$$T_{wb} = \frac{L}{v_x} = \frac{l_f + l_r}{v_x} \tag{18}$$

Thus, neglecting differences between the front and rear wheel tracks, the road disturbance experienced at the front axle corresponds to the road input subsequently encountered by the rear axle:

$$z_{r,r}(t + T_{wb}) \approx z_{r,f}(t) \tag{19}$$

The effective reconstruction delay τ_e accounts for both the reconstructed-road signal lag and the delay associated with transferring this information to the controller. The reconstructed road exhibits an approximately 15–16 ms peak-timing offset under the nominal 30 km/h condition. Using 16 ms as a representative reconstruction lag and conservatively allowing one reconstruction sampling interval of 1 ms and one controller update

interval of 5 ms, the effective delay is set to $\tau_e = 0.022$ s. This value represents a conservative timing allowance for causal preview control rather than an independently measured constant filter delay. The remaining usable preview interval after the estimate becomes available is therefore defined as

$$T_p = \max(0, T_{wb} - \tau_e) \tag{20}$$

The causal wheelbase-preview relationship used by the controller can be written as

$$\hat{z}^p_{r,r}\left(t + T_p\right) = \hat{z}_{r,f}(t) \tag{21}$$

where $\hat{z}^p_{r,r}$ denotes the predicted rear-road disturbance constructed from the previously observed front-road estimate.

This causal formulation is important because no rear-road estimate and no unmeasured future front-road profile are supplied to the proposed MPC. Instead, the controller stores the front-road estimate and shifts it according to the available wheelbase-preview interval. At each control instant k, the road-preview sequence supplied to the MPC is represented as

$$\mathbf{W}_p(k) = \begin{bmatrix} \hat{z}^p_{r,r}(k+1) \\ \hat{z}^p_{r,r}(k+2) \\ \vdots \\ \hat{z}^p_{r,r}(k+N_p) \end{bmatrix} \tag{22}$$

where N_p is the prediction horizon. The generation of the preview sequence and its incorporation into the closed-loop prediction model are described in Section 3.

The overall control architecture is shown in Figure 2. The baseline LQSOF controller provides continuous reactive stabilization using measured vehicle responses, while the proposed MPC generates an additive rear-axle command using the reconstructed wheelbase-preview information. Importantly, the two controllers are not treated as independent systems in the prediction stage. The LQSOF feedback dynamics and active-actuator response are embedded directly into the predictive plant, as developed in the following section.

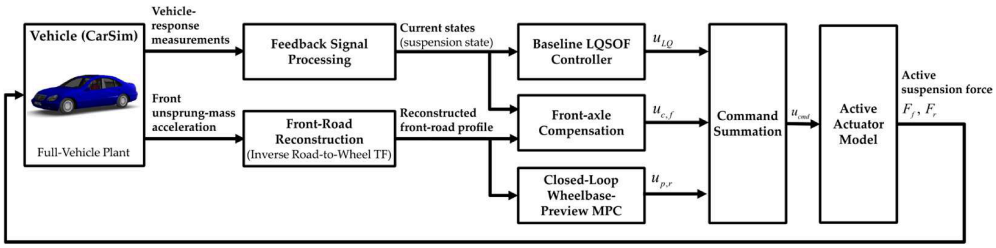


Figure 2. Overall architecture of the proposed closed-loop wheelbase-preview active-suspension control system using reconstructed front-road information.

3. Closed-Loop Wheelbase-Preview Model Predictive Control

The proposed controller uses reconstructed road information as an additional anticipatory input while retaining the LQSOF controller as the primary feedback layer. The front-road information reconstructed from the wheel response is used for the front-axle compensation defined in Section 2 and, after accounting for the wheelbase travel time, as causal preview information for the rear suspension. The MPC is therefore introduced only as an additional rear-axle preview layer rather than as a replacement for the existing feedback controller.

To determine the preview action consistently with the dynamics of the feedback-controlled suspension, the baseline LQSOF law and first-order actuator dynamics are incorporated directly into the prediction model. The resulting augmented model predicts

the interaction among the vehicle response, baseline feedback action, actuator-force dynamics, and rear preview input over the prediction horizon. Based on the causal rear-road sequence reconstructed from previously observed front-road information, the MPC optimizes the incremental additional rear-axle force. The control-effort penalty is applied only to this preview contribution, whereas the physical force constraint is imposed on the combined LQSOF and preview commands. The following subsections describe the closed-loop prediction model and the corresponding finite-horizon MPC formulation.

3.1. Closed-Loop Prediction Model

The control-oriented vehicle model introduced in Section 2 is written as

$$\dot{\mathbf{x}}_v = \mathbf{A}_v \mathbf{x}_v + \mathbf{B}_F \mathbf{F}_a + \mathbf{B}_w \mathbf{w} \tag{23}$$

where $\mathbf{x}_v$ is the eight-dimensional half-car state vector, $\mathbf{F}_a = [F_f \, F_r]^T$ contains the actual front- and rear-axle actuator forces, and $\mathbf{w} = [z_{r,f} \, z_{r,r}]^T$ represents the road disturbances acting on the two axles.

The baseline LQSOF controller is formulated using the pitch-plane half-car model introduced in Section 2. Using the LQSOF law defined in (14), the equivalent state-feedback representation for the closed-loop prediction model is written as

$$\begin{aligned} \mathbf{u}_{LQ} &= \mathbf{K}_x \mathbf{x}_v \\ \mathbf{K}_x &= -\mathbf{K}_{SOF} \mathbf{C}_y = \begin{bmatrix} \mathbf{k}_f^T \\ \mathbf{k}_r^T \end{bmatrix} \end{aligned} \tag{24}$$

where $\mathbf{k}_f$ and $\mathbf{k}_r$ denote the equivalent front- and rear-axle feedback gains, respectively. The same baseline LQSOF controller is retained without redesign so that the effect of the predictive wheelbase-preview layer can be evaluated independently of changes in the underlying feedback controller.

To account for the finite force-development dynamics defined in (10), the actual front- and rear-actuator forces are included in the augmented prediction state.

$$\mathbf{x}_a = \begin{bmatrix} \mathbf{x}_v^T & F_f & F_r \end{bmatrix}^T \tag{25}$$

Using the first-order actuator model introduced in Section 2, the actuator dynamics can be written compactly as

$$\dot{\mathbf{F}}_a = -\frac{1}{T_a}\mathbf{F}_a + \frac{1}{T_a}(\mathbf{K}_x \mathbf{x}_v + \mathbf{u}_{add}), \; \mathbf{u}_{add} = \begin{bmatrix} u_{c,f} \\ u_{p,r} \end{bmatrix} \tag{26}$$

where $\mathbf{u}_{add}$ is defined in (15), with $u_{c,f}$ representing the front road-compensation input and $u_{p,r}$ the optimized rear-preview input. The front compensation acts as a post-contact input because it becomes available only after the front wheel encounters the road disturbance, whereas the rear-preview input exploits the wheelbase travel time and can therefore act before the corresponding disturbance reaches the rear axle.

Substituting the baseline feedback law and actuator dynamics into the vehicle model yields

$$\dot{\mathbf{x}}_a = \mathbf{A}_{cl} \mathbf{x}_a + \mathbf{B}_p u_{p,r} + \mathbf{G}_f u_{c,f} + \mathbf{E}_a \mathbf{w} \tag{27}$$

where the augmented closed-loop system and input matrices are defined as

$$\mathbf{A}_{cl} = \begin{bmatrix} \mathbf{A}_v & \mathbf{B}_F \\ T_a^{-1}\mathbf{K}_x & -T_a^{-1}\mathbf{I}_2 \end{bmatrix}, \; \mathbf{B}_p = \begin{bmatrix} \mathbf{0}_{8\times1} \\ 0 \\ T_a^{-1} \end{bmatrix}, \; \mathbf{G}_f = \begin{bmatrix} \mathbf{0}_{8\times1} \\ T_a^{-1} \\ 0 \end{bmatrix}, \; \mathbf{E}_a = \begin{bmatrix} \mathbf{B}_w \\ \mathbf{0}_{2\times2} \end{bmatrix} \tag{28}$$

Here, $\mathbf{B}_p$ and $\mathbf{G}_f$ apply the additional rear-preview and front-compensation commands to the corresponding actuator-force states, respectively, while $\mathbf{E}_a$ introduces the front- and rear-road disturbances through the vehicle dynamics.

Equations (27) and (28) define the closed-loop prediction model by embedding the baseline LQSOF feedback law and actuator dynamics directly into the augmented system. Consequently, the future LQSOF action is not treated as an independent input but is recursively determined from the predicted vehicle state as

$$\mathbf{u}_{LQ}(k+i|k) = -\mathbf{K}_{SOF}\mathbf{C}_y\mathbf{x}_v(k+i|k),\ i = 1, \ldots, N_p \tag{29}$$

Thus, the optimized preview action affects both the predicted vehicle response and the subsequent baseline feedback action, allowing their interaction to be explicitly accounted for within the MPC prediction. This formulation follows the established feedback-embedded, pre-stabilized MPC principle, in which the baseline feedback law is incorporated into the prediction model [31,32]. In the present study, this principle is adapted to causal wheelbase-preview control using reconstructed road information, with the additional rear-preview force optimized while accounting for future LQSOF action and actuator-force dynamics and constraining the combined feedback and preview commands.

For digital implementation, the continuous-time model is discretized using a zero-order hold with the controller sampling interval T_s. The resulting model is

$$\mathbf{x}_a(k+1) = \mathbf{A}_d\mathbf{x}_a(k) + \mathbf{B}_d u_{p,r}(k) + \mathbf{G}_d u_{c,f}(k) + \mathbf{E}_d\mathbf{w}(k) \tag{30}$$

where $\mathbf{A}_d$, $\mathbf{B}_d$, $\mathbf{G}_d$, and $\mathbf{E}_d$ are obtained by zero-order-hold discretization of the continuous-time augmented model as

$$\begin{aligned} &\mathbf{A}_d = e^{\mathbf{A}_{cl}T_s} \\ &[\mathbf{B}_d\ \mathbf{G}_d\ \mathbf{E}_d] = \int_0^{T_s} e^{\mathbf{A}_{cl}\tau}\left[\mathbf{B}_p\ \mathbf{G}_f\ \mathbf{E}_a\right]d\tau \end{aligned} \tag{31}$$

The road-disturbance matrix is partitioned as $\mathbf{E}_d = [\mathbf{E}_{d,f}\ \mathbf{E}_{d,r}]$, corresponding to the front- and rear-road inputs.

In the finite-horizon prediction, however, future front-road information is not assumed to be available because no forward-looking road sensor is used. Therefore, the predicted road-disturbance vector contains only the causal rear-road preview constructed from the stored front-road information:

$$\hat{\mathbf{w}}^p(k+i \mid k) = \begin{bmatrix} 0 \\ \hat{z}^p_{r,r}(k+i \mid k) \end{bmatrix} \tag{32}$$

In the nominal prediction model, the unknown future front-road disturbance is set to zero because no forward-looking road measurement is available. This assumption does not imply that the physical front-road excitation vanishes immediately after the current control instant. In particular, when the longitudinal disturbance length exceeds the vehicle wheelbase, overlapping front- and rear-axle excitation may introduce errors in the predicted coupled heave–pitch response.

The zero-input assumption also avoids extrapolating potentially uncertain reconstructed-road information. Since the road elevation is estimated using an inverse transfer function, the reconstructed signal may contain errors associated with measurement noise and model mismatch. Maintaining the latest estimated road elevation throughout the prediction horizon would repeatedly introduce such errors into the predicted disturbance sequence, potentially affecting the predicted vehicle response and optimized control forces. Setting the unknown future front-road input to zero avoids this additional extrapolation assumption but does not eliminate errors caused by continuing road excitation.

The measured vehicle states, embedded LQSOF feedback dynamics, and available front compensation input are retained in the prediction model. Thus, the zero-input assumption applies only to the unavailable future front-road disturbance.

Using the available preview interval T_p defined in (20), the reconstructed front-road signal is stored in a history buffer and shifted to construct the causal rear-road preview sequence. For the i-th step of the prediction horizon, the required delay in discrete samples and the corresponding rear-road preview are defined as

$$\begin{aligned} d_i &= \mathrm{round}\left(\tfrac{T_p - iT_s}{T_s}\right) \\ \hat{z}^p_{r,r}(k+i \mid k) &= \begin{cases} \hat{z}_{r,f}(k-d_i), & d_i \geq 0 \\ 0, & d_i < 0 \end{cases} \end{aligned} \tag{33}$$

When $d_i \geq 0$, the required disturbance value already exists in the stored history of the reconstructed front-road signal and can therefore be supplied to the MPC without violating causality. When $d_i < 0$, the corresponding value would require future front-road information that has not yet been observed. The disturbance is therefore set to zero rather than being extrapolated. Accordingly, the proposed formulation does not require a separately reconstructed rear-road signal or measured future front-road information. Unknown future road-disturbance samples are set to zero in the nominal prediction model rather than being extrapolated from the available estimates. The resulting rear-road samples, obtained exclusively from road excitation already encountered at the front axle, are assembled over the prediction horizon to form a causal time-domain disturbance preview for the MPC.

3.2. MPC Formulation

Using the discrete-time closed-loop system in (30), the future augmented states are recursively predicted over a horizon of N_p sampling intervals. The stacked prediction can be expressed in the standard lifted form as

$$\mathbf{X}_k = \mathbf{S}_x \mathbf{x}_a(k) + \mathbf{S}_u \mathbf{U}_{p,k} + \mathbf{S}_g \mathbf{G}_k + \mathbf{S}_w \mathbf{W}_k \tag{34}$$

Here, $\mathbf{X}_k$ contains the predicted augmented states, whereas $\mathbf{U}_{p,k}$ contains the additional rear-preview commands over the prediction horizon. They are defined as

$$\mathbf{X}_k = \begin{bmatrix} \mathbf{x}_a(k+1 \mid k) \\ \mathbf{x}_a(k+2 \mid k) \\ \vdots \\ \mathbf{x}_a(k+N_p \mid k) \end{bmatrix}, \ \mathbf{U}_{p,k} = \begin{bmatrix} u_{p,r}(k \mid k) \\ u_{p,r}(k+1 \mid k) \\ \vdots \\ u_{p,r}(k+N_p-1 \mid k) \end{bmatrix} \tag{35}$$

Because future front-road information is not available, the prediction does not assume a future sequence of front-compensation inputs. Only the front-compensation command available at the current control instant is included, and its future values are set to zero:

$$\mathbf{G}_k = \begin{bmatrix} u_{c,f}(k) & 0 & \dots & 0 \end{bmatrix}^T \tag{36}$$

The causal rear-road preview sequence introduced in Section 2.2 is embedded into the two-channel road-disturbance structure of the discrete prediction model. Because future front-road information is unavailable, the front-road component of each predicted disturbance vector is set to zero, yielding

$$\mathbf{W}_k = \begin{bmatrix} 0 \\ \hat{z}^p_{r,r}(k \mid k) \\ 0 \\ \hat{z}^p_{r,r}(k+1 \mid k) \\ \vdots \\ 0 \\ \hat{z}^p_{r,r}(k+N_p-1 \mid k) \end{bmatrix} \tag{37}$$

The prediction matrices are constructed directly from the discrete-time matrices in (30). Rather than expanding the complete block-Toeplitz matrices, their block elements are defined as

$$\begin{aligned} [\mathbf{S}_x]_i &= \mathbf{A}_d^i, \quad i = 1, \ldots, N_p \\ [\mathbf{S}_u]_{ij} &= \begin{cases} \mathbf{A}_d^{i-j}\mathbf{B}_d, & j \le i \\ \mathbf{0}, & j > i \end{cases} \\ [\mathbf{S}_g]_{ij} &= \begin{cases} \mathbf{A}_d^{i-j}\mathbf{G}_d, & j \le i \\ \mathbf{0}, & j > i \end{cases} \\ [\mathbf{S}_w]_{ij} &= \begin{cases} \mathbf{A}_d^{i-j}\mathbf{E}_d, & j \le i \\ \mathbf{0}, & j > i \end{cases} \end{aligned} \tag{38}$$

Thus, $\mathbf{S}_w$ retains the full front- and rear-road disturbance structure of $\mathbf{E}_d$, while the corresponding future front-road entries in $\mathbf{W}_k$ are zero. The lifted formulation therefore uses only road information that is causally available from the reconstructed front-road history.

Rather than independently optimizing the absolute rear preview force at every future step, the proposed controller adopts the preview-force increment as the decision variable. The absolute command sequence is reconstructed according to

$$\mathbf{U}_{p,k} = \mathbf{1}_{N_p} u_p(k-1) + \mathbf{T}\Delta\mathbf{U}_k \tag{39}$$

where $\mathbf{1}_{Np}$ denotes an N_p-dimensional column vector of ones, $\Delta\mathbf{U}_k$ contains the future preview-force increments, and $\mathbf{T}$ is a lower-triangular accumulation matrix.

The incremental formulation serves two purposes. First, it allows the rate of change of the additive preview command to be constrained explicitly. Second, it discourages rapid variations in the optimized force when a localized road disturbance enters or exits the prediction horizon. This is particularly useful when the optimized command is implemented through an actuator with finite force-development dynamics.

The finite-horizon cost function is defined as

$$J = \sum_{i=1}^{N_p} \mathbf{x}_{i|k}^T \mathbf{Q}_x \mathbf{x}_{i|k} + \sum_{i=1}^{N_p} r_u \overline{u}_{p,i|k}^2 + \sum_{i=1}^{N_c} r_{\Delta u} \Delta\overline{u}_{p,i|k}^2 \tag{40}$$

where N_c denotes the control horizon, r_u penalizes the magnitude of the additive preview force, and $r_{\Delta u}$ penalizes its variation.

The state-weighting matrix is constructed from the selected vehicle-performance outputs. In the present formulation, the performance-output vector includes the sprung-mass vertical acceleration, pitch angle, pitch rate, and pitch acceleration and is defined as

$$\mathbf{y}_p = \begin{bmatrix} \ddot{z}_c & \theta & \dot{\theta} & \ddot{\theta} \end{bmatrix}^T = \mathbf{C}_p \mathbf{x}_a \tag{41}$$

The corresponding output matrix is expressed as

$$\mathbf{C}_p = \begin{bmatrix} \mathbf{C}_{a_z} \\ \mathbf{C}_\theta \\ \mathbf{C}_{\dot{\theta}} \\ \mathbf{C}_{\ddot{\theta}} \end{bmatrix} \tag{42}$$

where the individual output rows are obtained from the augmented vehicle model as

$$\begin{aligned}\mathbf{C}_{a_z} &= \begin{bmatrix} [\mathbf{A}_v]_{5,:} & [\mathbf{B}_F]_{5,:} \end{bmatrix} \\ \mathbf{C}_{\theta} &= \begin{bmatrix} \mathbf{e}_2^T & \mathbf{0}_{1\times 2} \end{bmatrix} \\ \mathbf{C}_{\dot{\theta}} &= \begin{bmatrix} \mathbf{e}_6^T & \mathbf{0}_{1\times 2} \end{bmatrix} \\ \mathbf{C}_{\ddot{\theta}} &= \begin{bmatrix} [\mathbf{A}_v]_{6,:} & [\mathbf{B}_F]_{6,:} \end{bmatrix}\end{aligned} \tag{43}$$

Here, $\mathbf{e}_i$ denotes the i-th unit vector associated with the vehicle-state vector $\mathbf{x}_v$. The performance-output scaling matrix is defined as

$$\mathbf{S}_p = \mathrm{diag}\left(s_{a_z}, s_{\theta}, s_{\dot{\theta}}, s_{\ddot{\theta}}\right) \tag{44}$$

and the normalized performance output is given by

$$\overline{\mathbf{y}}_p = \mathbf{S}_p^{-1}\mathbf{y}_p = \overline{\mathbf{C}}_p\mathbf{x}_a, \;\; \overline{\mathbf{C}}_p = \mathbf{S}_p^{-1}\mathbf{C}_p \tag{45}$$

The weighting matrix for the normalized performance outputs is defined as

$$\mathbf{W}_p = \mathrm{diag}\left(w_{a_z}, w_{\theta}, w_{\dot{\theta}}, w_{\ddot{\theta}}\right) \tag{46}$$

and the resulting state-weighting matrix is

$$\mathbf{Q}_x = \overline{\mathbf{C}}_p^T\mathbf{W}_p\overline{\mathbf{C}}_p \tag{47}$$

The additive rear-preview force and its increment are normalized in the same manner as

$$\overline{u}_{p,r} = \frac{u_{p,r}}{s_u}, \;\; \Delta\overline{u}_{p,r} = \frac{\Delta u_{p,r}}{s_{\Delta u}} \tag{48}$$

where s_u and $s_{\Delta u}$ denote the preview-force and preview-force-increment scale factors, respectively.

The weighting coefficients determine the relative emphasis placed on vertical ride response and body-pitch suppression. Because the performance outputs are normalized by different scale factors, the numerical magnitude of an individual weight does not alone determine its contribution to the optimization objective. Furthermore, the cost minimizes multiple coupled vehicle-response terms together with penalties on the magnitude and increment of the additional preview force, rather than a single ride-comfort measure. The acceleration outputs are obtained from the augmented vehicle model and explicitly depend on the actuator-force states F_f and F_r. Thus, the performance cost is evaluated using the actuator forces predicted after the first-order actuator dynamics rather than the ideal commanded forces.

The control-effort penalty is applied only to the additive preview command, since the baseline LQSOF action is already embedded in the closed-loop prediction model. In contrast, the physical actuator constraint is imposed on the combined LQSOF and preview commands because both are realized through the same actuator.

Accordingly, the predicted total rear-axle command is constrained as

$$\left|\mathbf{k}_r^T\mathbf{x}_v(k+i|k) + u_{p,i|k}\right| \le u_{\max}, \quad i = 1, \ldots, N_p \tag{49}$$

In addition, the magnitude and rate of the preview contribution itself are constrained according to

$$\left|u_{p,i|k}\right| \le u_{p,\max}, \quad \left|\Delta u_{p,i|k}\right| \le \Delta u_{p,\max} \tag{50}$$

These constraints restrict the predictive layer from producing unrealistically large or rapidly varying additional forces and prevent it from overwhelming the baseline feedback controller.

The substitution of the lifted prediction model (34) and the incremental-input representation (39) into the cost function (40) results in a constrained quadratic optimization problem of the form

$$\min_{\Delta \mathbf{U}_k} \frac{1}{2}\Delta \mathbf{U}_k^T \mathbf{H} \Delta \mathbf{U}_k + \mathbf{f}_k^T \Delta \mathbf{U}_k \quad \text{s.t.} \quad \mathbf{A}_{ineq} \Delta \mathbf{U}_k \leq \mathbf{b}_{ineq} \tag{51}$$

where $\mathbf{H}$ and $\mathbf{f}_k$ are determined from the prediction matrices and weighting terms, whereas $\mathbf{A}_{ineq}$ and $\mathbf{b}_{ineq}$ collect the additive-force, force-rate, and total-actuator constraints. The explicit expressions of $\mathbf{H}$, $\mathbf{f}_k$, $\mathbf{A}_{ineq}$, and $\mathbf{b}_{ineq}$ are omitted because they follow directly from the lifted prediction model, cost function, and constraints defined above.

At each control update, the reconstructed rear-road preview sequence is evaluated against an activation threshold of 0.001 m. Specifically, QP optimization is bypassed when the maximum absolute value of the predicted rear-road samples is below this threshold. The baseline LQSOF controller and front-road compensation remain active regardless of this bypass condition. Otherwise, the constrained QP is solved using the current vehicle state, actuator-force states, and reconstructed-road history. Following the receding-horizon principle, only the first optimized input increment is applied.

$$u_p(k) = u_p(k-1) + \Delta u_p^*(k|k) \tag{52}$$

The remaining elements of the optimized sequence are discarded, and the preview activation condition is evaluated again at the next control update. When optimization is bypassed, no QP solver call is performed, and the rear-preview command is driven toward zero subject to the specified preview-force-increment limit. Under the laterally symmetric road condition considered in this study, the resulting rear-axle preview force is distributed equally to the left and right rear suspension actuators.

Overall, the proposed control architecture retains the LQSOF controller as the baseline feedback layer, while the MPC optimizes only the additional rear-axle preview force. Because the baseline feedback law and actuator dynamics are explicitly embedded in the prediction model, the preview action is determined according to the predicted closed-loop response during the available wheelbase-preview interval. The actuator-command constraint is imposed on the combined feedback and preview commands and is enforced when a valid constrained QP solution is obtained. The treatment of unsuccessful optimization is discussed separately in Section 4.4.5.

4. Results

4.1. Simulation Environment and Evaluation Conditions

The proposed controller was evaluated using a co-simulation environment integrating CarSim 2017.1 and MATLAB/Simulink R2023b. CarSim was employed as the full-vehicle simulation plant, whereas MATLAB/Simulink implemented the baseline LQSOF controller, reconstructed-road processing, wheelbase-preview generation, and the proposed MPC. Both the baseline LQSOF controller and the MPC prediction model were formulated using the same control-oriented pitch-plane half-car model introduced in Section 2. Under the laterally symmetric road condition considered in this study, the axle-level control commands were distributed equally to the corresponding left- and right-side suspension actuators of the CarSim vehicle. The same control-oriented model was used for both LQSOF and MPC so that the effect of the additional predictive wheelbase-preview layer could be evaluated without changing the underlying feedback-control model. The left- and right-side suspension parameters of the full-vehicle model were combined to obtain the corresponding equivalent axle-level parameters for the pitch-plane half-car model. The CarSim full-vehicle plant was based on an E-Class sedan model, with selected vehicle parameters modified using Genesis G80 specifications. The principal vehicle parameters are summarized in Table 1.

Table 1. Principal parameters of the target vehicle and control-oriented half-car model.

Parameter	Symbol	Value
Sprung mass	m_s	1925.49 kg
Front unsprung mass	$m_{u,f}$	85.24 kg
Rear unsprung mass	$m_{u,r}$	85.24 kg
Pitch moment of inertia	I_y	3736.09 kg·m^2
Distance from CG to front axle	l_f	1.420 m
Distance from CG to rear axle	l_r	1.590 m
Wheelbase	L	3.010 m
Front suspension stiffness	$k_{s,f}$	96,000 N/m
Rear suspension stiffness	$k_{s,r}$	104,000 N/m
Front suspension damping coefficient	b_f	3528 N·s/m
Rear suspension damping coefficient	b_r	3528 N·s/m
Front tire vertical stiffness	$k_{t,f}$	460,000 N/m
Rear tire vertical stiffness	$k_{t,r}$	460,000 N/m

A laterally symmetric bump with a height of 0.10 m and a nominal longitudinal length of 3.6 m was used at vehicle speeds of 20, 30, 40, 50, and 60 km/h, with 30 km/h as the nominal condition. For the 3.01 m wheelbase, the corresponding wheelbase travel times are approximately 0.542, 0.361, 0.271, 0.217, and 0.181 s. The nominal usable preview intervals are 0.520, 0.339, 0.249, 0.195, and 0.159 s after subtracting the 0.022 s reconstruction allowance defined in Section 2.2. Bump-length sensitivity was evaluated at 30 km/h using lengths of 1.8, 3.6, and 7.2 m with the same height and TF-MPC settings, as described in Section 4.4.6.

The CarSim full-vehicle model was simulated with a 1 ms integration step. The LQ-SOF and MPC controllers were updated every 5 ms, while the reconstructed-road signal was processed at a sampling interval of 1 ms. Each active suspension actuator was implemented in Simulink using the first-order command-to-force dynamics defined in Section 2.1. The resulting actuator output force was applied to the corresponding suspension corner of the CarSim full-vehicle model. The nominal time constant was 0.0199 s, representing an assumed force-response bandwidth of approximately 8 Hz. The sensitivity to deviations from this nominal actuator response is examined separately in Section 4.4.2. Therefore, the controller command was passed through the actuator dynamics before the resulting suspension force was applied to the full-vehicle model.

The MPC weights, normalization scales, and input constraints were maintained unchanged across the investigated vehicle speeds. Both prediction and control horizons were fixed at $N_p = N_c = 150$ steps with a 5 ms controller sampling interval, corresponding to a 0.75 s prediction window. This horizon was selected considering the finite wheelbase-preview interval available from the reconstructed front-road information. For the 3.01 m wheelbase, the front-to-rear travel times are approximately 0.542, 0.361, and 0.271 s at 20, 30, and 40 km/h, respectively. Thus, the 150-step horizon covers the entire causally available rear-road preview interval at all evaluated speeds, even after accounting for the nominal reconstruction and scheduling delay. Longer prediction horizons do not provide additional measured road-preview information, although they may affect the optimization through subsequent vehicle and actuator dynamics. In the investigated simulations, reducing the horizons to 150 steps produced no appreciable change in the reported suspension-performance indices compared with the longer-horizon configurations. The fixed horizon was therefore adopted to reduce computational complexity while maintaining the observed control performance. The simulation and controller parameters are summarized in Table 2.

Table 2. Simulation and controller parameters used for performance evaluation.

Item	Symbol	Condition
Full-vehicle plant	—	Modified E-Class sedan model in CarSim (selected parameters based on Genesis G80)
Controller model	—	Pitch-plane half-car model
Simulation environment	—	CarSim–MATLAB/Simulink co-simulation
Road disturbance	—	Symmetric bump
Bump height	—	0.10 m
Bump length	—	3.6 m
Vehicle speeds	v_x	20, 30, 40, 50, and 60 km/h
Nominal vehicle speed	$v_{x,nom}$	30 km/h
CarSim/plant simulation step	—	1 ms
MPC/LQSOF control sampling time	T_s	5 ms
Road-reconstruction sampling time	—	1 ms
Prediction horizon	N_p	150
Control horizon	N_c	150
Effective road-reconstruction delay	τ_e	0.022 s
Actuator model	—	First-order force response
Actuator time constant	T_a	0.0199 s
Vertical-acceleration weight	ω_{az}	70
Pitch-angle weight	ω_θ	50
Pitch-rate weight	$\omega_{\dot\theta}$	25
Pitch-acceleration weight	$\omega_{\ddot\theta}$	2
Additive preview-force weight	r_u	20
Preview-force-increment weight	$r\Delta_u$	40
Vertical-acceleration scale	s_{az}	2.0 m/s^2
Pitch-angle scale	s_θ	0.020 rad
Pitch-rate scale	$s_{\dot\theta}$	0.12 rad/s
Pitch-acceleration scale	$s_{\ddot\theta}$	1.0 rad/s^2
Preview-force scale	s_u	2500 N/axle
Preview-force-increment scale	$s_{\Delta u}$	300 N/axle
Additive preview-force limit	$u_{p,\max}$	±3600 N/axle
Preview-force-increment limit	$\Delta u_{p,\max}$	±360 N/update
Total actuator-command limit	$u_{\max}$	±10,000 N/axle

The output weights in Table 2 set the intended emphasis on vertical acceleration and pitch regulation after normalization. The scale factors are reference magnitudes rather than hard performance limits. Separate penalties on preview-force magnitude and increment discourage excessive effort and abrupt command changes. The preview-force, increment, and total-command limits distinguish the additional MPC contribution from the combined actuator demand. These values define a common nominal tuning, whose input-penalty sensitivity is examined in Section 4.4.4.

Six suspension configurations were compared. The passive case was used as the uncontrolled reference, whereas the LQSOF case represented the reactive-feedback baseline without road-preview information. It should be noted that LQ Preview is supplied with the exact road profile, whereas TF Preview and TF-MPC rely on the same reconstructed front-road information. Therefore, LQ Preview serves as an idealized reference rather than a directly comparable implementation using the same road-information source. The TF Preview controller converted this reconstructed road information into rear wheelbase-preview action using a proportional control law, whereas TF-MPC employed the proposed closed-loop predictive formulation to optimize the additional rear-preview force. The configurations are summarized in Table 3.

Table 3. Controller configurations and nominal gain settings used for comparison.

Controller	Road Information	Control Configuration	Nominal Gain or Parameter
Passive	None	No active control	—
LQSOF	None	Static output feedback	$\mathbf{K}_{\mathrm{SOF,4c}}$
LQ Preview	True road profile	LQ optimal preview	LQ preview design in Ref. [15]
TF Preview	Reconstructed road	Proportional preview	$K_{c,f} = -193.524$ N/m $K_{p,r} = 5814.643$ N/m
Front TF Only	Reconstructed road	Proportional preview for front only	$K_{c,f} = -193.524$ N/m
TF-MPC	Reconstructed road	Closed-loop MPC	$\mathbf{K}_{\mathrm{SOF,4c}}$, $K_{c,f} = -193.524$ N/m; MPC weights in Table 2

$\mathbf{K}_{\mathrm{SOF,4c}}$ is defined as follows:

$$\mathbf{K}_{\mathrm{SOF,4c}} = 10^3 \begin{bmatrix} \mathbf{K}_1 & \mathbf{K}_2 \end{bmatrix}$$
$$\mathbf{K}_1 = \begin{bmatrix} -6.6368 & 1.2258 & -9.8686 & 0 & 0 \\ 6.6368 & 1.2258 & 0 & -9.8686 & 0 \\ -6.6368 & -9.7491 & 0 & 0 & -9.8686 \\ 6.6368 & -9.7491 & 0 & 0 & 0 \end{bmatrix} \tag{53}$$
$$\mathbf{K}_2 = \begin{bmatrix} 0 & 2.4538 & 0 & 0 & 0 \\ 0 & 0 & 2.4538 & 0 & 0 \\ 0 & 0 & 0 & 2.4538 & 0 \\ -9.8686 & 0 & 0 & 0 & 2.4538 \end{bmatrix}$$

TF Preview and TF-MPC use the same road-reconstruction method but determine the rear-preview action through proportional compensation and constrained optimization, respectively. Their comparison evaluates the two implemented preview strategies, whereas the controlled prediction-model ablation in Section 4.4.1 examines the individual architectural components.

A Front TF Only configuration is included to distinguish front-road compensation from rear-preview control. It retains the LQSOF controller and front compensation used in TF-MPC, while the additional rear command is disabled. Comparison with TF-MPC therefore evaluates the effect of enabling the rear predictive-control layer under the same baseline-feedback and front-compensation configuration.

The proportional rear-compensation gain is evaluated at factors of 0, 0.5, 1.0, 1.5, and 2.0 relative to its nominal value at 20, 30, and 40 km/h. The front compensation is retained throughout the sweep. Zero corresponds to Front TF Only, and unity corresponds to the nominal TF Preview controller. All tested gains are reported because the gain minimizing the pitch-angle RMS does not necessarily minimize the pitch-rate or vertical-acceleration RMS. The sweep evaluates the tested gain range and is not presented as a global tuning optimization.

The online quadratic program was solved using MATLAB's quadprog solver with the active-set algorithm. Computational performance was evaluated on a workstation equipped with an Intel Core i9-11900K CPU and an NVIDIA GeForce RTX 5070 GPU, with the QP optimization performed entirely on the CPU without GPU acceleration. The corresponding computation-time results are presented in Section 4.4.5.

Suspension performance was evaluated using the RMS and peak-to-peak sprung-mass vertical acceleration as ride-response indices and the RMS pitch angle and pitch rate as measures of body-motion suppression. Rear suspension stroke and tire deflection were additionally examined as evaluation metrics for suspension travel and tire–road response but were not directly included in the MPC objective. The Actuator-force RMS was calculated by pooling the squared samples of the four-individual actuator-force signals actually applied

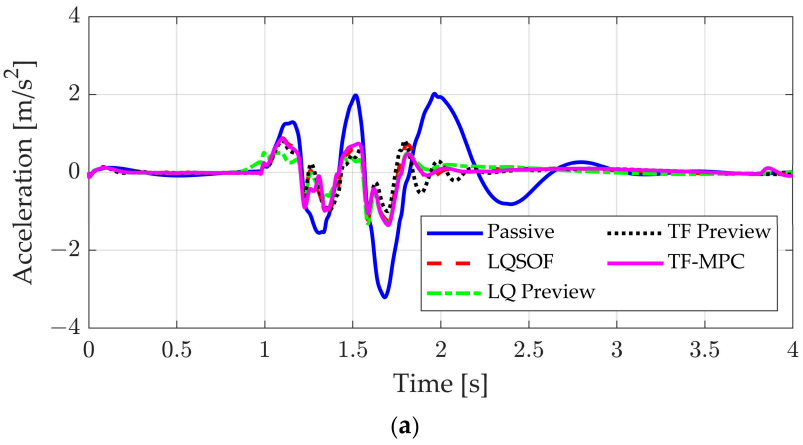
to the vehicle and taking the square root of their mean. Thus, it is a per-corner pooled RMS, not the RMS of the summed four-corner force. Rear-axle output force is the sum of the two rear actuator forces. Unless otherwise stated, all RMS indices were calculated over the complete simulation interval.

These indices provide a consistent quantitative basis for evaluating vertical vibration suppression and pitch-attitude regulation across the investigated suspension controllers. For a more comprehensive assessment of occupant ride comfort, complementary metrics such as the ISO 2631-1 [33] frequency-weighted acceleration RMS and vibration dose value (VDV) may be considered to account for human sensitivity to vibration. Such occupant-oriented measures, preferably evaluated at the occupant-supporting surface, represent an extension of the vehicle-body response evaluation adopted in the present study.

4.2. Nominal Bump-Crossing Performance

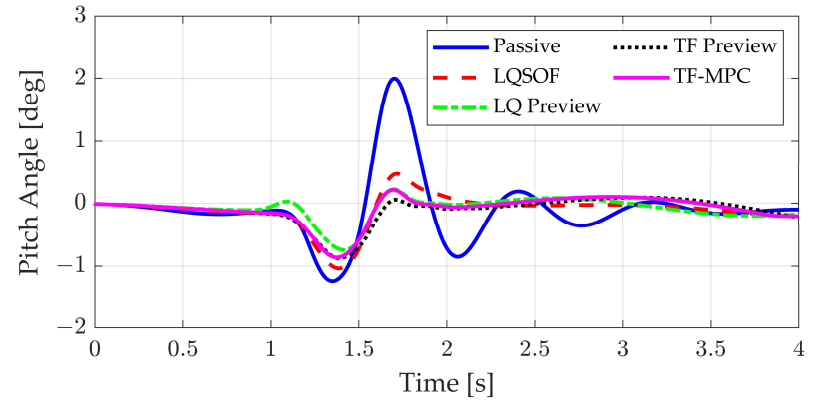
Figure 3 compares the transient responses of the five suspension configurations at the nominal vehicle speed of 30 km/h. The passive suspension exhibits the largest vertical-acceleration, pitch-angle, and pitch-rate excursions, together with pronounced oscillations following the front- and rear-wheel passages over the bump. In contrast, all active-control cases substantially suppress the body responses and shorten the duration of the post-bump oscillations. The preview-based controllers further modify the transient response around the bump-crossing event compared with the feedback-only LQSOF controller. In particular, TF Preview produces relatively small vertical-acceleration and pitch-rate responses at this nominal speed, whereas TF-MPC provides stronger suppression of the pitch-angle response while maintaining a comparable overall vertical-response level. The rear-axle actuator force in Figure 3d also shows that the preview controllers reshape the control action relative to the LQSOF baseline, reflecting the additional rear-preview contribution introduced by each strategy. These qualitative differences in the transient responses are quantified using the RMS and peak-to-peak performance indices summarized in Table 4.

Relative to the passive suspension, TF-MPC reduced the RMS vertical acceleration from 0.767 to 0.291 m/s^2, corresponding to a reduction of approximately 62.1%, while the peak-to-peak vertical acceleration was reduced by 57.5%. The RMS pitch angle and pitch rate were also reduced by 55.5% and 70.3%, respectively. These results demonstrate that the proposed controller substantially suppresses both vertical and pitch responses compared with the uncontrolled suspension.

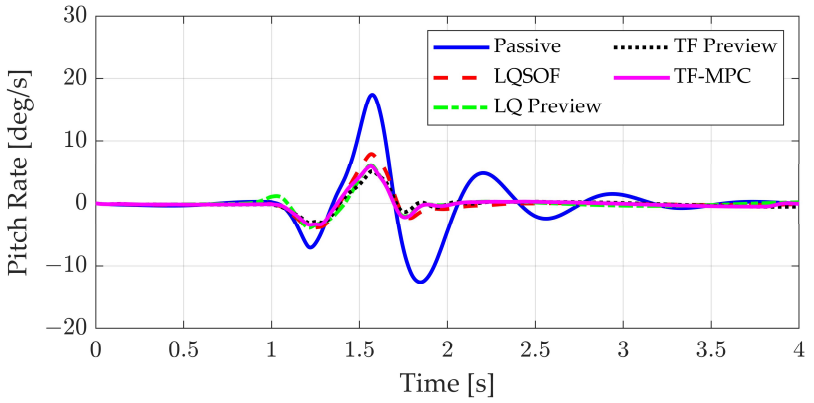


(**a**)

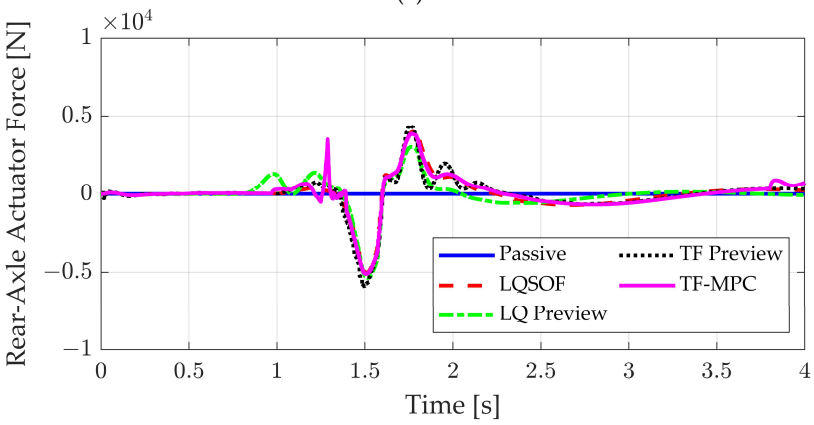
Figure 3. *Cont.*



(**b**)



(**c**)



(**d**)

Figure 3. Comparison of vehicle responses at 30 km/h: (**a**) sprung-mass vertical acceleration, (**b**) pitch angle, (**c**) pitch rate, and (**d**) rear-axle actuator force.

Table 4. Suspension performance at 30 km/h.

Controller	Vertical Acc. RMS [m/s²]	Vertical Acc. P2P [m/s²]	Pitch RMS [deg]	Pitch Rate RMS [deg/s]	Actuator Force RMS [N]
Passive	0.767	5.233	0.509	4.132	–
LQSOF	0.288	2.121	0.274	1.618	405.9
LQ Preview	0.259	1.828	0.189	1.236	397.5
TF Preview	0.258	1.818	0.257	1.084	466.8
TF-MPC	0.291	2.224	0.226	1.226	459.2

At 30 km/h, TF-MPC reduced the pitch-angle and pitch-rate RMS relative to LQSOF by 17.5% and 24.3%, respectively. This improvement was accompanied by increases in the vertical-acceleration RMS from 0.2876 to 0.2908 m/s^2 (1.1%) and peak-to-peak acceleration from 2.1212 to 2.2241 m/s^2 (4.8%). The actual actuator-force RMS increased from 405.9 to 459.2 N (13.1%). These results show the nominal trade-off between pitch regulation, vertical response, and actuation effort in the normalized multi-objective formulation. Relative to TF Preview, TF-MPC reduced the pitch-angle RMS by 12.0% and the actual actuator-force RMS by 1.6%, while the vertical-acceleration and pitch-rate RMS increased by 12.7% and 13.1%. The predictive layer therefore changes the balance among the response indices rather than minimizing each index independently.

To examine whether these changes in body response are accompanied by changes in suspension travel or tire–road response, Figure 4 compares the rear suspension stroke and tire deflection for the five suspension configurations.

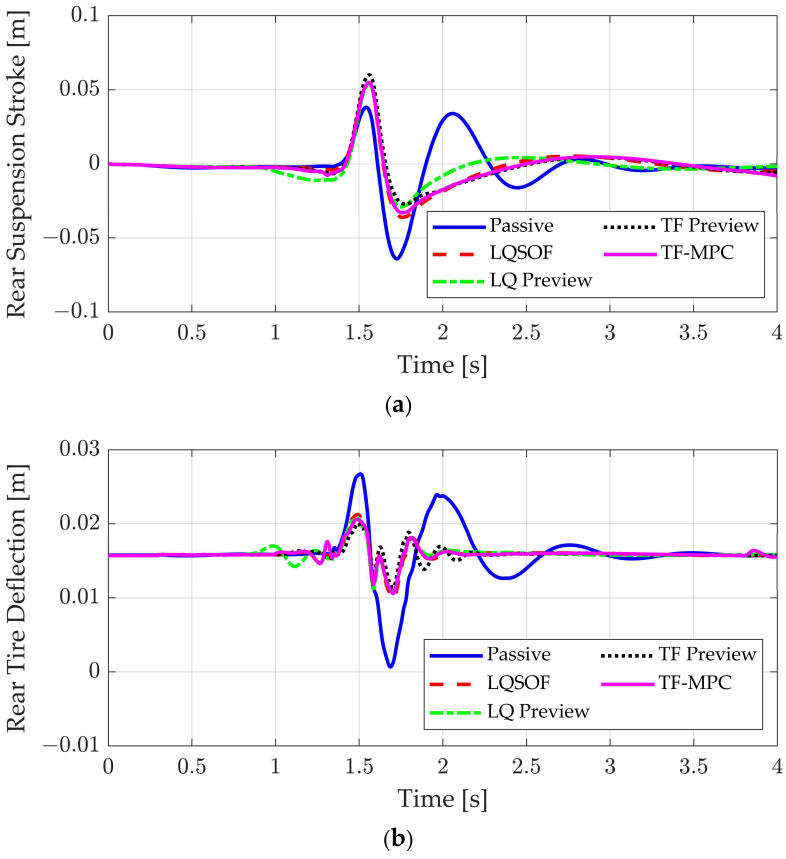


Figure 4. Rear suspension responses at 30 km/h: (**a**) rear suspension stroke and (**b**) rear tire deflection.

At 30 km/h, the RMS rear suspension stroke of TF-MPC was 12.00 mm, compared with 11.43 mm for TF Preview, corresponding to an increase of approximately 5.0%. In contrast, the RMS rear tire deflection differed by less than 0.1% between the two controllers. This result indicates a modest increase in suspension travel associated with the improved pitch-angle suppression of TF-MPC, while the tire-deflection response remains essentially unchanged.

Figure 5 further illustrates the control structure of TF-MPC by decomposing the rear-axle command into the baseline LQSOF component, the additional MPC preview component, and their combined command.

The RMS rear-axle LQSOF command was approximately 1064 N, whereas the additional MPC preview component had an RMS value of approximately 320 N. The preview

contribution was therefore substantially smaller than the baseline feedback command. Because the two components were not generally in phase, the combined rear-axle command had an RMS value of approximately 1124 N, only 5.6% higher than the baseline rear command. The RMS magnitude of the additional preview component was approximately 30% of that of the baseline LQSOF command. These results confirm that the MPC operates as an additive preview layer that modifies the existing feedback action rather than replacing the baseline controller.

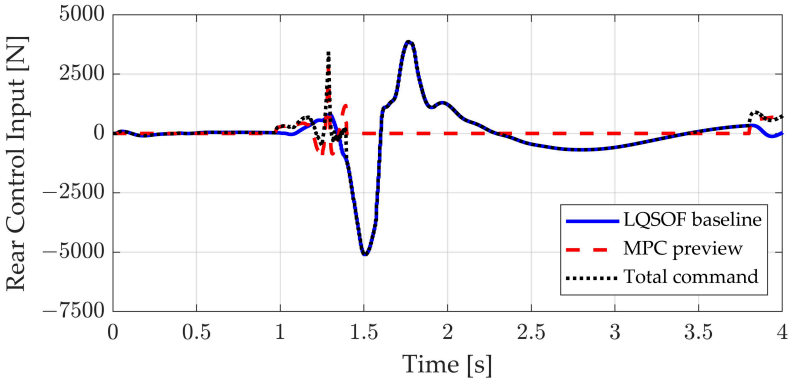


Figure 5. Decomposition of the rear-axle command for the proposed TF-MPC controller at 30 km/h.

4.3. Suspension Performance at Different Vehicle Speeds

The suspension performance was evaluated at 20, 30, and 40 km/h using the same 0.10 m high, 3.6 m long bump. For the 3.01 m wheelbase considered in this study, the nominal front-to-rear wheelbase travel times are 0.542, 0.361, and 0.271 s at 20, 30, and 40 km/h, respectively. The MPC weighting coefficients, actuator constraints, and prediction and control horizons were maintained unchanged across the investigated speeds. At a sampling interval of 5 ms, the fixed 150-step horizon corresponds to 0.75 s, covering the available wheelbase-preview interval at all three speeds. Figure 6 compares the principal suspension configurations in terms of the sprung-mass vertical-acceleration RMS, pitch-angle RMS, pitch-rate RMS, and actual actuator-force RMS. Table 5 provides the corresponding numerical results, including the front-compensation-only configuration and the proportional rear-gain sensitivity analysis.

Relative to LQSOF, the complete TF-MPC configuration reduced the pitch-angle RMS by 11.7%, 17.5%, and 9.5% at 20, 30, and 40 km/h, respectively. The corresponding pitch-rate RMS reductions were 22.0%, 24.3%, and 18.9%. In contrast, the vertical-acceleration RMS increased slightly by 0.5% and 1.1% at 20 and 30 km/h, respectively, and decreased by 0.6% at 40 km/h. These results demonstrate improved pitch-attitude regulation relative to the baseline feedback controller, although a consistent reduction in vertical acceleration was not achieved.

To distinguish the contribution of rear MPC from that of front-road compensation, the proposed controller was compared with the Front TF Only configuration, which retains LQSOF and the same front compensation while disabling the additional rear command. At 20 and 30 km/h, the inclusion of rear MPC reduced the pitch-angle RMS by 16.0% and 11.8% and the pitch-rate RMS by 4.5% and 1.5%, respectively. The corresponding vertical-acceleration RMS values differed by less than 0.1%, while actual actuator-force RMS decreased by 1.8% and 0.8%. At 40 km/h, however, TF-MPC increased the pitch-angle, pitch-rate, and vertical-acceleration RMS by 11.1%, 2.2%, and 7.4%, respectively, relative to Front TF Only. These results indicate that the additional rear predictive-control layer provides a measurable pitch-regulation benefit at 20 and 30 km/h, but its contribution is not uniformly favorable across the investigated speeds.

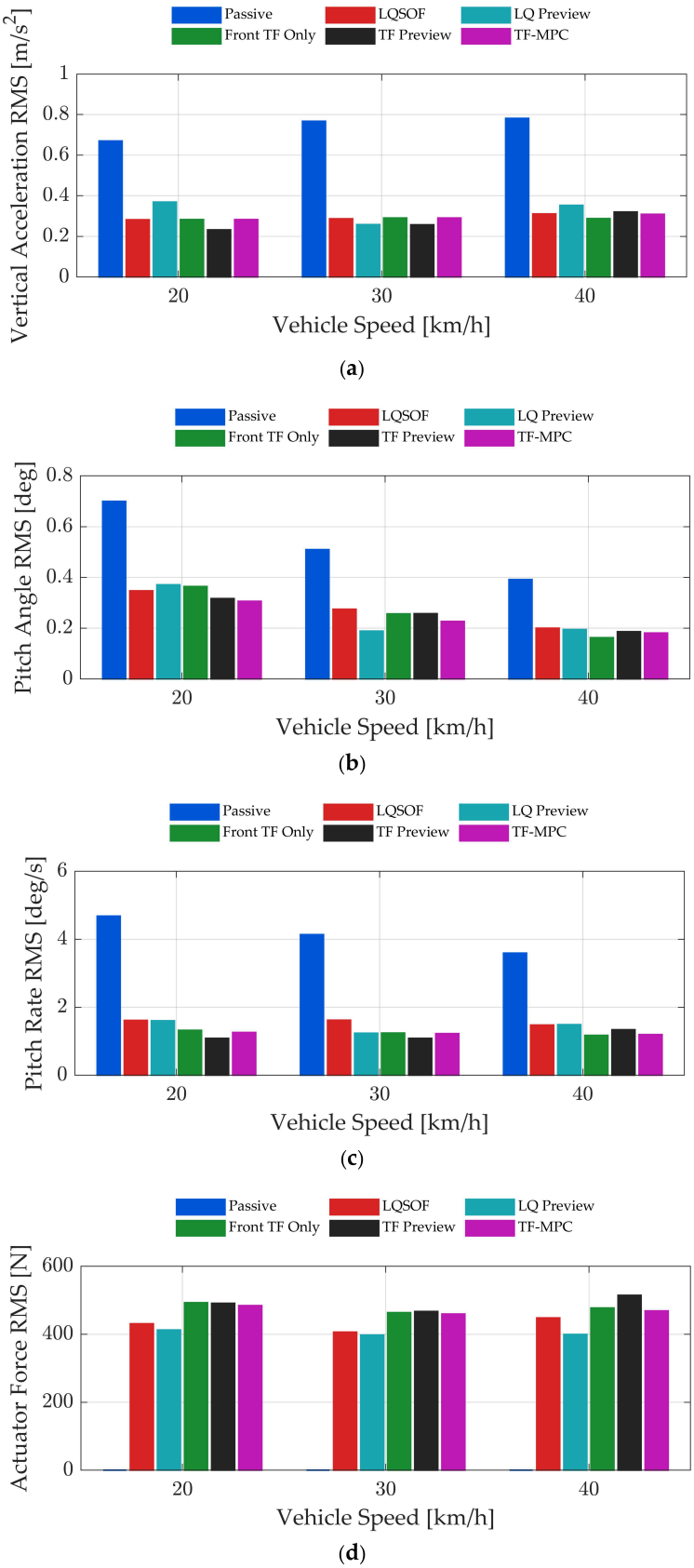


Figure 6. Comparison of suspension performance under the investigated 20–40 km/h bump-crossing conditions: (**a**) vertical-acceleration RMS, (**b**) pitch-angle RMS, (**c**) pitch-rate RMS, and (**d**) actual actuator-force RMS.

Table 5. Suspension performance at 20, 30, and 40 km/h: comparison of LQSOF, front-only TF compensation, TF Preview with different rear-gain factors, and TF-MPC.

Speed [km/h]	Controller	Vertical Acc. RMS [m/s^2]	Pitch RMS [deg]	Pitch Rate RMS [deg/s]	Actuator Force RMS [N]
20	LQSOF	0.2823	0.3467	1.6170	430.8
	Front TF Only	0.2838	0.3643	1.3220	492.5
	TF Preview (0.5)	0.2836	0.3471	1.2919	472.2
	TF Preview (1.0)	0.2326	0.3169	1.0828	490.3
	TF Preview (1.5)	0.2812	0.3890	1.3518	519.0
	TF Preview (2.0)	0.2797	0.4274	1.4038	555.6
	TF-MPC	0.2837	0.3060	1.2620	483.8
30	LQSOF	0.2876	0.2745	1.6185	405.9
	Front TF Only	0.2906	0.2567	1.2441	463.0
	TF Preview (0.5)	0.2904	0.2560	1.2320	451.0
	TF Preview (1.0)	0.2581	0.2572	1.0841	466.8
	TF Preview (1.5)	0.2867	0.2625	1.2459	483.0
	TF Preview (2.0)	0.2849	0.2790	1.2651	506.6
	TF-MPC	0.2908	0.2264	1.2259	459.2
40	LQSOF	0.3109	0.2000	1.4797	448.0
	Front TF Only	0.2876	0.1629	1.1746	477.0
	TF Preview (0.5)	0.2904	0.1698	1.1691	471.3
	TF Preview (1.0)	0.3209	0.1861	1.3402	514.0
	TF Preview (1.5)	0.2926	0.1597	1.1662	499.5
	TF Preview (2.0)	0.2944	0.1655	1.1726	520.0
	TF-MPC	0.3090	0.1810	1.2000	468.1

The sensitivity of proportional rear-preview compensation was further examined by varying the rear gain from 0 to 2.0 times its nominal value, using factors of 0, 0.5, 1.0, 1.5, and 2.0 while retaining the front compensation. The zero-gain case corresponds to Front TF Only, whereas unity represents the nominal TF Preview controller. As summarized in Table 5, the proportional controller exhibits speed- and metric-dependent responses. At 20 km/h, the nominal rear gain yielded the lowest pitch-angle and pitch-rate RMS among the tested proportional configurations. At 30 km/h, the lowest pitch-angle RMS occurred at a gain factor of 0.5, whereas the lowest pitch-rate RMS occurred at the nominal gain. At 40 km/h, a gain factor of 1.5 provided the lowest values for both pitch indices. Accordingly, the gain producing the most favorable response depends on the operating condition and performance criterion.

Compared with nominal TF Preview, TF-MPC reduced the pitch-angle RMS by 3.4% and 12.0% at 20 and 30 km/h, respectively, while reducing the actual actuator-force RMS by 1.3% and 1.6%. However, TF Preview achieved lower vertical-acceleration and pitch-rate RMS values under these conditions. Notably, TF-MPC produced a lower pitch-angle RMS than all tested proportional rear-gain configurations at both speeds. At 40 km/h, the proportional controller with a gain factor of 1.5 achieved lower vertical-acceleration, pitch-angle, and pitch-rate RMS values than TF-MPC, whereas TF-MPC required a 6.3% lower actual actuator-force RMS. Thus, the proposed controller provides condition-dependent pitch-regulation benefits but does not uniformly outperform proportional preview compensation across all response indices.

Overall, the results demonstrate that reconstructed-road wheelbase-preview control can improve pitch-attitude regulation without requiring a forward-looking road sensor. The additional contribution of rear MPC is evident at 20 and 30 km/h, whereas at 40 km/h, the proportional and front-compensation-only configurations provide more favorable body responses for the tested conditions. Because vehicle speed also changes the temporal excitation associated with the fixed spatial bump, these differences cannot be attributed solely

to the available wheelbase-preview interval. To examine the effect of the effective-delay setting under a fixed excitation condition, an additional sensitivity analysis is presented in Section 4.4.8.

4.4. Performance and Sensitivity Analyses

4.4.1. Ablation Study of the Closed-Loop Prediction Model

To isolate the contributions of future feedback prediction and actuator-force dynamics, an ablation study was conducted under the nominal bump-crossing condition at 30 km/h. Two variants of TF-MPC were considered: one excluding future LQSOF feedback prediction (No FB Pred.) and another neglecting actuator dynamics in the prediction model (No Act. Dyn.). In both variants, the baseline LQSOF controller and the physical actuator dynamics in the simulation plant were retained, while the corresponding components were omitted from the MPC prediction model. The road-reconstruction method, MPC weighting coefficients, input constraints, and prediction and control horizons of 150 steps were maintained consistently across the configurations.

Figure 7 compares the time responses of the three MPC configurations, while Table 6 summarizes their RMS performance together with the LQSOF and TF Preview reference controllers.

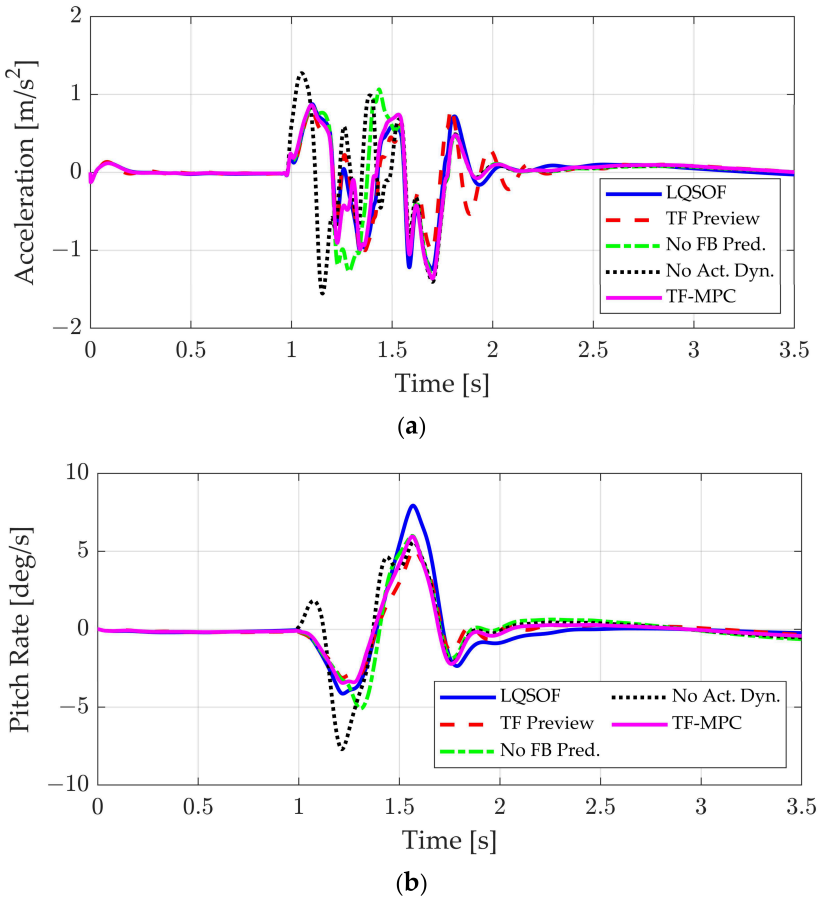


Figure 7. Comparison of transient responses for the TF-MPC ablation study at 30 km/h: (**a**) sprung-mass vertical acceleration and (**b**) pitch rate. "No FB Pred." and "No Act. Dyn." Denote TF-MPC variants without future LQSOF feedback prediction and without actuator dynamics in the prediction model, respectively.

Compared with the variants excluding future feedback prediction and actuator dynamics, the complete TF-MPC reduced the vertical-acceleration RMS by 13.3% and 16.4%,

the pitch-angle RMS by 28.9% and 30.2%, and the pitch-rate RMS by 13.9% and 28.5%, respectively. Under common MPC settings, these comparisons substantiate the contributions of the two prediction-model components. The broader controller trade-off at 30 km/h remains as reported in Section 4.2: TF Preview gives lower vertical-acceleration and pitch-rate RMS values, whereas TF-MPC gives a lower pitch-angle RMS.

Table 6. Ablation study of the closed-loop prediction model at 30 km/h.

Controller	Vertical Acc. RMS [m/s^2]	Pitch RMS [deg]	Pitch Rate RMS [deg/s]
LQSOF	0.2876	0.2745	1.6185
TF Preview	0.2581	0.2572	1.0841
TF-MPC without future feedback prediction	0.3354	0.3184	1.4236
TF-MPC without actuator dynamics	0.3480	0.3242	1.7141
Complete TF-MPC	0.2908	0.2264	1.2259

4.4.2. Sensitivity to Actuator Model Mismatch

To investigate the sensitivity of TF-MPC to actuator-model uncertainty, the actual actuator time constant was varied to 0.5, 1.5, and 2.0 times its nominal value of 0.0199 s. The MPC prediction matrices, constructed using the nominal actuator dynamics, were kept unchanged for all cases. The simulations were conducted at 30 km/h with $N_p = N_c = 150$.

Table 7 summarizes the resulting suspension performance. Compared with the nominal condition, the vertical-acceleration RMS increased by 2.2%, 4.3%, and 2.6% for the respective time-constant variations. Although variations were also observed in the pitch responses, the overall results indicate limited sensitivity to the investigated actuator-model mismatches under the nominal bump-crossing condition.

Table 7. Sensitivity to actuator time-constant mismatch at 30 km/h.

$T_a/T_{a,\mathrm{nom}}$	Vertical Acc. RMS [m/s^2]	Pitch RMS [deg]	Pitch Rate RMS [deg/s]
0.5	0.2972	0.2533	1.3211
1.0	0.2908	0.2264	1.2259
1.5	0.3033	0.2302	1.2412
2.0	0.2984	0.2401	1.2631

4.4.3. Road Reconstruction Accuracy and Sensitivity

The accuracy and robustness of the reconstructed front-road profile were evaluated by comparing the estimated road elevation with the true road input obtained from CarSim. Figure 8 compares the reconstructed profiles under different filtering and noise conditions at 30 km/h, while Table 8 summarizes the corresponding root-mean-square error (RMSE), correlation coefficient, peak-amplitude error, and peak-timing difference.

Table 8. Road reconstruction accuracy under different estimation conditions at 30 km/h.

Condition	RMSE (mm)	Correlation	Peak Error (%)	Peak Delay (ms)	Pre-Bump RMS (mm)
Nominal (HPF ON)	14.65	0.968	−12.06	15	0.00
HPF OFF	13.11	0.973	−8.67	16	0.00
Low Noise	12.17	0.971	−4.50	16	2.02
High Noise	10.13	0.971	+3.12	16	4.08

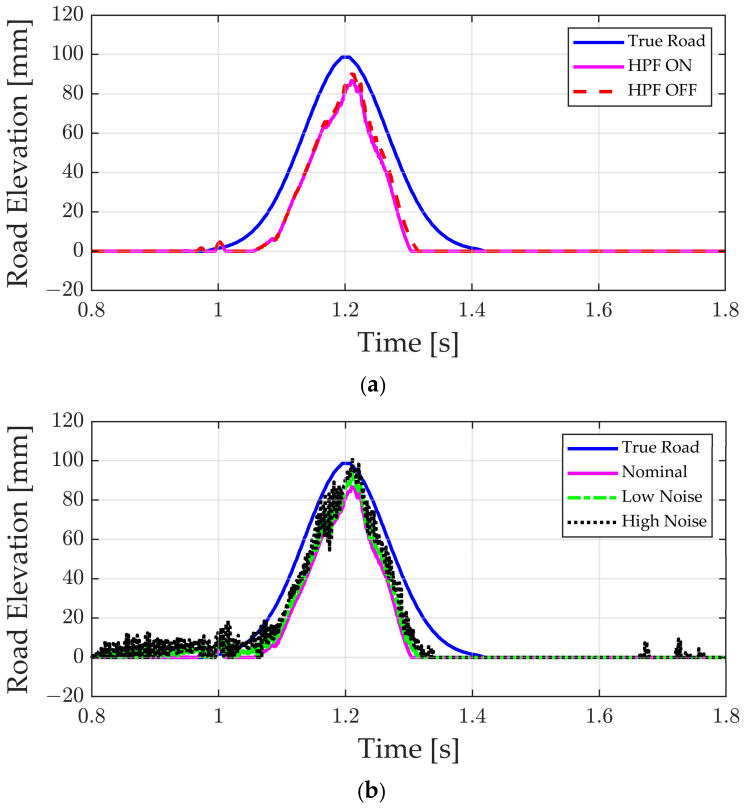


Figure 8. Comparison of true and reconstructed front-road profiles at 30 km/h: (**a**) effect of high-pass filtering and (**b**) sensitivity to noise.

To evaluate measurement-noise sensitivity, band-limited white noise was added to the front-wheel vertical-acceleration measurement before road reconstruction. The Simulink Band-Limited White Noise block was configured with a noise-power parameter of 0.005, a sampling interval of 0.01 s, and a fixed random seed value of 23341 specified in the block settings. The Low Noise and High Noise conditions were generated by applying gains of 0.5 and 1.0, respectively, to the same noise realization. The road-reconstruction model retained its original sampling interval of 1 ms. The smooth and Class A/B road inputs described in Section 2.2 were used for transfer-function identification, not independent stochastic-road closed-loop performance validation.

Under the nominal condition, the reconstructed road profile achieved an RMSE of 14.65 mm and a correlation coefficient of 0.968. Disabling the high-pass filter reduced the RMSE to 13.11 mm, while the peak-timing difference remained nearly unchanged. Under the Low Noise and High Noise conditions, the RMSE values were 12.17 and 10.13 mm, respectively, whereas the pre-bump RMS fluctuations increased to 2.02 and 4.08 mm. The lower RMSE values observed for these particular noise conditions should not be interpreted as a general improvement in reconstruction accuracy with increasing measurement noise. Instead, the increasing pre-bump fluctuations indicate the sensitivity of the reconstructed signal to measurement noise. The observed peak-timing offset of 15–16 ms is distinct from the conservative effective delay of 22 ms used for wheelbase-preview scheduling, as explained in Section 2.2.

To further investigate the sensitivity of road reconstruction to vehicle-model uncertainty, the sprung mass of the CarSim vehicle model was varied by ±200 and ±400 kg at 40 km/h, while the nominal inverse transfer function remained unchanged. As summarized in Table 9, the reconstruction RMSE ranged from 12.521 to 12.600 mm, compared with 12.567 mm under the nominal condition, corresponding to a maximum relative deviation

of approximately 0.37%. The correlation coefficients remained approximately 0.955, while the peak-amplitude errors and peak-timing differences ranged from 6.79% to 8.03% and from 20 to 22 ms, respectively. These results indicate limited sensitivity to the investigated sprung-mass variations, although the effects of other vehicle-parameter uncertainties require further investigation. The 22 ms delay used for preview scheduling is a nominal allowance calibrated at 30 km/h. The measured peak offsets in Table 9 illustrate that reconstruction timing depends on the operating condition; the scheduling allowance is not a universal measured filter delay.

Table 9. Sensitivity of road-profile reconstruction to sprung-mass variations at 40 km/h.

Condition	RMSE (mm)	Correlation	Peak Error (%)	Peak Delay (ms)
−400 kg	12.521	0.9552	+8.03	20
−200 kg	12.552	0.9552	+7.98	21
Nominal	12.567	0.9553	+7.71	21
+200 kg	12.583	0.9553	+7.05	21
+400 kg	12.600	0.9552	+6.79	22

To further evaluate the influence of measurement noise on closed-loop suspension performance, the proposed TF-MPC controller was examined under four road-reconstruction conditions at 30 km/h: Nominal (HPF ON), HPF OFF, Low Noise, and High Noise. The same 0.10 m high, 3.6 m long bump and unchanged MPC parameters were used throughout the comparison. The measurement-noise configurations were identical to those described in the preceding reconstruction-accuracy analysis.

Figure 9 compares the corresponding sprung-mass vertical acceleration, pitch angle, pitch rate, and actual actuator-force responses. Table 10 summarizes the RMS values calculated over the complete simulation interval. The actuator-force RMS was computed from the actual output forces of all four suspension actuators.

Table 10. Closed-loop sensitivity of TF-MPC to road-reconstruction and measurement-noise conditions at 30 km/h.

Condition	Vertical Acc. RMS (m/s^2)	Pitch RMS (deg)	Pitch Rate RMS (deg/s)	Actual Force RMS (N)
Nominal (HPF ON)	0.2908	0.2264	1.2259	459.2
HPF OFF	0.2931	0.2519	1.2276	446.3
Low Noise	0.2936	0.2360	1.2189	444.1
High Noise	0.2757	0.2615	1.2560	492.9

Under Low Noise, the vertical-acceleration and pitch-angle RMS increased by 0.9% and 4.2%, respectively, while the pitch-rate RMS and actual actuator-force RMS decreased by 0.6% and 3.3%, respectively, relative to the nominal condition.

Under High Noise, the vertical-acceleration RMS decreased by 5.2%, whereas the pitch-angle RMS, pitch-rate RMS, and actual actuator-force RMS increased by 15.5%, 2.5%, and 7.3%, respectively. These results indicate that measurement noise affects the individual performance metrics differently. In particular, the reduction in the vertical-acceleration RMS under High Noise should not be interpreted as a general improvement in ride comfort because pitch regulation and actuator demand deteriorated under the same condition.

Disabling the HPF increased the pitch-angle RMS by 11.3% compared with the nominal filtered case while reducing the actuator-force RMS by 2.8%. This comparison illustrates a trade-off between reconstruction filtering, vehicle-body motion, and actuator effort. The HPF-off configuration is included as a finite-duration sensitivity case rather than an independently stable reconstruction implementation.

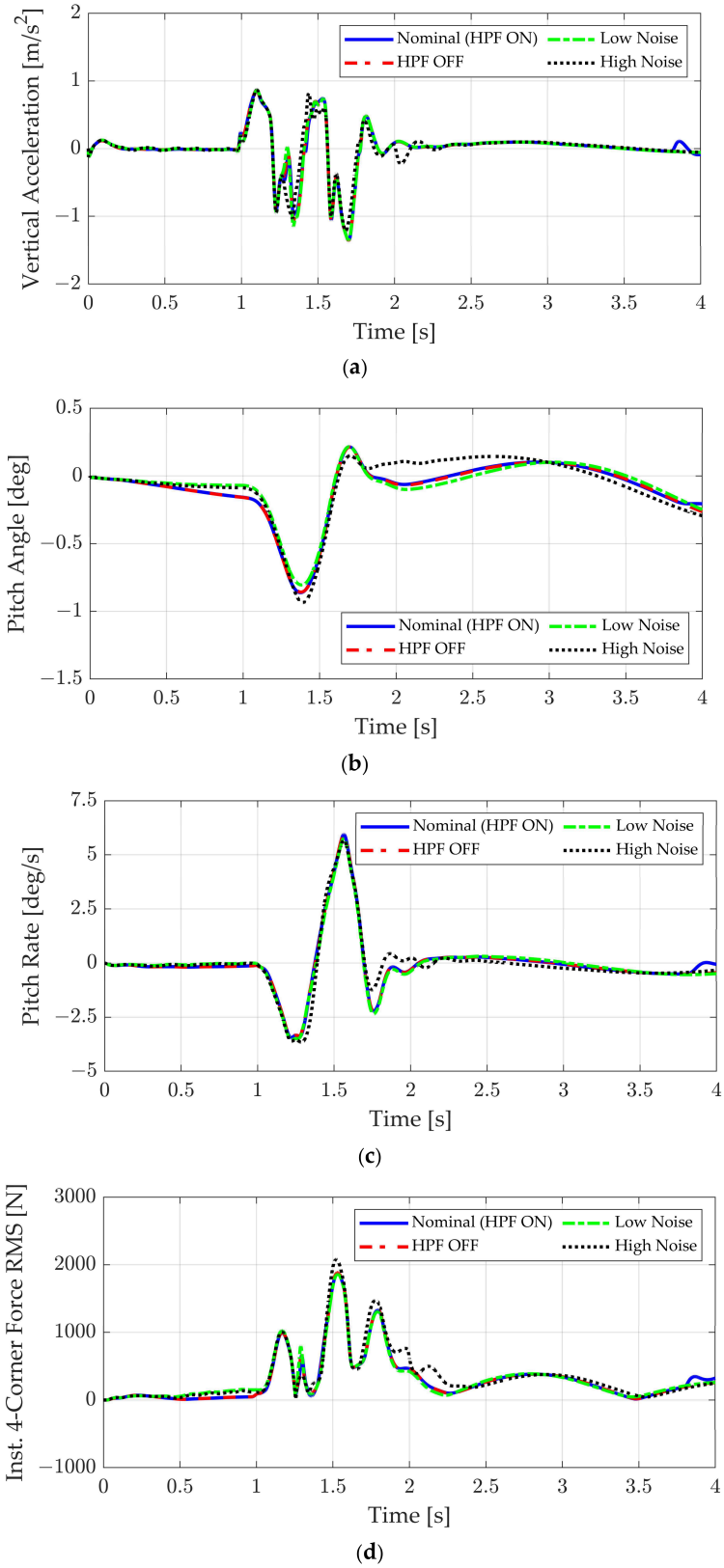


Figure 9. Closed-loop responses of TF-MPC under different road-reconstruction and measurement-noise conditions at 30 km/h (Nominal, HPF OFF, Low Noise, and High Noise): (**a**) sprung-mass vertical acceleration, (**b**) pitch angle, (**c**) pitch rate, and (**d**) instantaneous RMS of the four actual actuator forces.

The results demonstrate the influence of the investigated measurement-noise conditions on both road reconstruction and closed-loop vehicle responses. However, the analysis

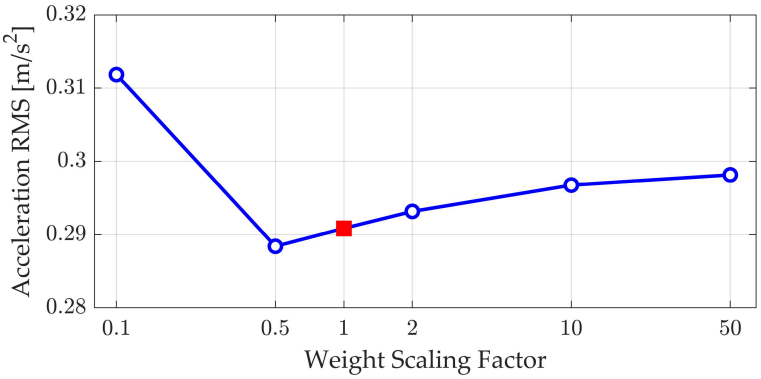
is limited to the evaluated bump and noise realization, and the findings should not be generalized to independent stochastic-road conditions or other vehicle speeds without further validation.

4.4.4. Sensitivity to MPC Weighting Parameters

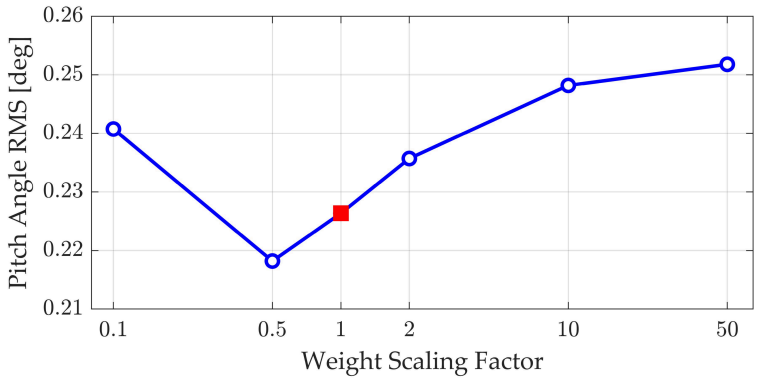
The additive preview-force and preview-force-increment weights were jointly scaled by factors of 0.1, 0.5, 1, 2, 10, and 50 relative to the nominal values at 30 km/h. All other MPC settings, including the 150-step horizons, were fixed. This one-dimensional sweep examines the balance between body response and additional control effort.

As shown in Figure 10, a scaling factor of 0.5 reduced the vertical-acceleration and pitch-angle RMS by 0.8% and 3.6%, respectively, while increasing the actual actuator-force RMS by 3.8%. A factor of 10 reduced the actuator-force RMS by 3.4% but increased the pitch-angle RMS by 9.6%. Increasing the factor to 50 provided little further force reduction. At 0.1, the vertical-acceleration, pitch-angle, and actuator-force RMS increased by 7.2%, 6.3%, and 14.9%, respectively.

The nominal weights represent a compromise between body-response regulation and actuator effort within the investigated parameter range. Although the input-penalty variations did not reduce the vertical-acceleration RMS below the LQSOF reference at 30 km/h, the results demonstrate the sensitivity of the vertical and pitch responses to the selected control penalties. Since only the preview-force and preview-force-increment weights were varied, alternative output-weight distributions may provide different performance balances. A broader multi-objective weighting optimization is beyond the scope of the present sensitivity analysis.



(**a**)



(**b**)

Figure 10. *Cont.*

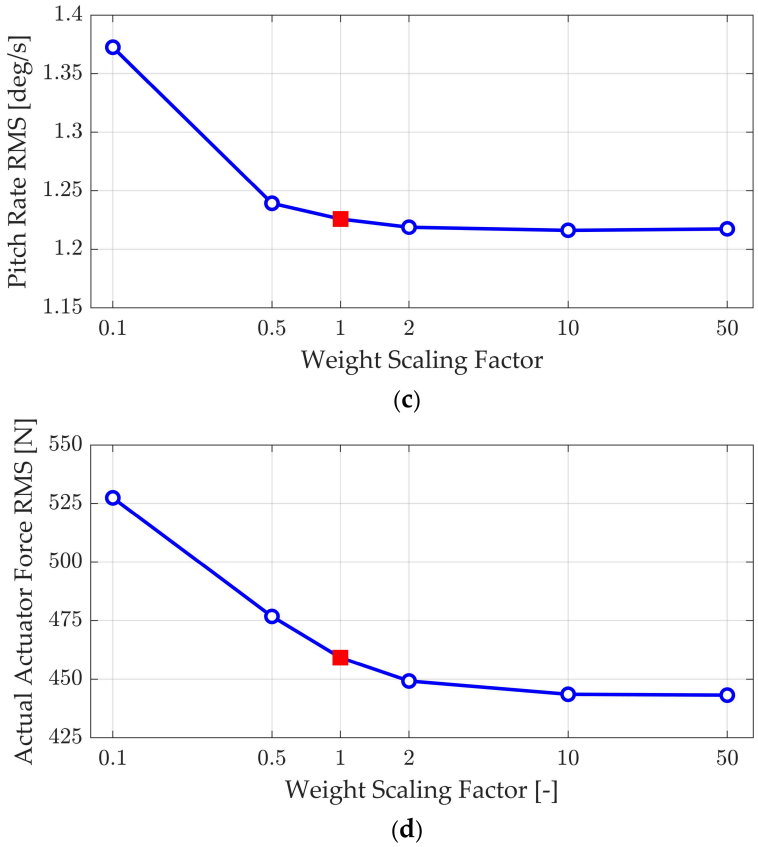


Figure 10. Sensitivity of TF-MPC performance to simultaneous scaling of the preview-force and preview-force-increment weights at 30 km/h: (**a**) vertical-acceleration RMS, (**b**) pitch-angle RMS, (**c**) pitch-rate RMS, and (**d**) actual actuator-force RMS. The red squares indicate the nominal reference condition at a weighting scale factor of 1.0, and the line segments connect the evaluated data points to illustrate the trends.

4.4.5. Computational Performance of Online Optimization

The QP execution time was evaluated under the nominal 30 km/h condition using fixed 150-step prediction and control horizons at a 5 ms control period. The evaluated Mode-2 interval corresponds to the operating period in which the additive rear-preview MPC configuration was enabled. During this interval, 188 MPC control updates were recorded, of which 73 bypassed optimization because the reconstructed rear-road preview remained below the activation threshold. Consequently, the QP solver was invoked 115 times, and all QP calls were successfully solved, yielding a solver-success rate of 100%. No unsuccessful QP calls or solver-availability errors occurred during the evaluated interval.

The mean, median, 99th-percentile, and maximum QP execution times were 1.1313, 0.7595, 2.8221, and 3.8740 ms, respectively. All recorded QP execution times were below the 5 ms control period. The timing statistics include only actual QP solver calls, excluding control updates at which optimization was bypassed. These measurements demonstrate solver-level timing compliance within the evaluated operating interval, rather than a complete-loop or startup worst-case execution bound.

In addition to QP optimization, the complete control algorithm requires inverse-TF- and HPF-based road reconstruction at a 1 ms sampling interval, followed by preview-sequence generation and updates of the state- and disturbance-dependent QP terms at each 5 ms control instant. The preview alignment can be updated according to the current vehicle speed using the wheelbase travel time in Equation (18), the available preview interval in Equation (20), and the discrete delay indices in Equation (33). Because the vehicle and

actuator prediction model and the prediction and control horizons are fixed, the lifted prediction matrices do not explicitly depend on vehicle speed and need not be recomputed solely due to speed variations. Instead, the preview sequence and corresponding optimization data are updated according to the available road information and current vehicle states. However, the computational overhead of these additional operations was not independently measured, and the present constant-speed simulations do not establish the performance of this update strategy under continuous acceleration or deceleration. Complete-loop timing and variable-speed implementation therefore require further validation.

Solver timing and constrained-solution success are assessed separately. At 50 and 60 km/h, unsuccessful constrained QP solves occurred together with saturation of the additional rear-preview command, even after increasing the permitted iterations. These cases are therefore excluded from the principal comparison of successfully solved constrained-MPC performance.

Commands generated following an unsuccessful optimization are distinguished from valid constrained QP solutions. In particular, limiting a fallback command does not establish satisfaction of all constraints over the prediction horizon. Consequently, computation-time compliance is not used as evidence of QP feasibility. Any reported feasible-solve rate refers only to the specified operating conditions and actual optimization attempts, excluding updates at which the preview gate bypassed the QP.

4.4.6. Sensitivity to Bump Length

Bump lengths of 1.8, 3.6, and 7.2 m were evaluated at 30 km/h with a fixed height of 0.10 m and unchanged TF-MPC parameters. The nominal usable wheelbase-preview interval remained 0.339 s, while bump-crossing duration changed to 0.216, 0.432, and 0.864 s, respectively. Table 11 compares Passive, LQSOF, TF Preview, and TF-MPC.

Table 11. Sensitivity of suspension performance to longitudinal bump length at 30 km/h.

Bump Length	Controller	Vertical Acc. RMS [m/s^2]	Pitch RMS [deg]	Pitch Rate RMS [deg/s]	Actuator Force RMS [N]
1.8 m	Passive	0.5389	0.2763	2.2816	0
	LQSOF	0.4685	0.1812	0.7704	406.8
	TF Preview	0.4898	0.1691	0.7694	426.5
	TF-MPC	0.4632	0.1876	0.8401	424.9
3.6 m	Passive	0.7671	0.5091	4.1319	0
	LQSOF	0.2876	0.2745	1.6185	405.9
	TF Preview	0.2581	0.2572	1.0841	466.8
	TF-MPC	0.2908	0.2264	1.2259	459.2
7.2 m	Passive	0.8198	0.6466	4.9629	0
	LQSOF	0.2459	0.3302	1.4585	550.5
	TF Preview	0.2428	0.3296	1.4793	590.0
	TF-MPC	0.2410	0.2881	1.4781	576.3

For the 3.6 and 7.2 m bumps, TF-MPC reduced the pitch-angle RMS relative to LQSOF by 17.5% and 12.7%, respectively. The vertical-acceleration RMS remained close to LQSOF across all lengths, ranging from a 1.1% increase to a 2.0% reduction. For the 1.8 m bump, TF-MPC reduced the vertical-acceleration RMS by 1.1% relative to LQSOF and by 5.4% relative to TF Preview, but the pitch-angle and pitch-rate RMS were higher than for both active references.

The short-bump peak-to-peak acceleration was 5.042 m/s^2 for TF-MPC, compared with 5.261 for LQSOF and 5.686 for TF Preview, giving reductions of 4.2% and 11.3%, respectively.

It remained 2.5% above the passive value of 4.918 m/s^2. The actual actuator-force RMS was higher than LQSOF but lower than TF Preview for each tested bump length.

The results identify a disturbance-dependent trade-off: pitch-angle regulation is improved for the nominal and longer bumps, whereas the shortest bump favors vertical-response suppression over pitch suppression. These observations characterize the fixed controller under localized bump excitation; they do not isolate actuator bandwidth as the sole cause of the differences or establish broadband stochastic-road robustness.

4.4.7. Sensitivity to Future Front-Road Prediction

The influence of the future front-road disturbance assumption was investigated by comparing the nominal zero-input prediction with an alternative hold-last prediction at 20, 30, and 40 km/h. In the hold-last configuration, the latest reconstructed front-road elevation was maintained throughout the prediction horizon, while the causal rear wheelbase-preview formulation was retained. Both configurations used identical MPC weights, actuator models, constraints, and fixed prediction and control horizons of 150 steps.

Table 12 summarizes the resulting suspension-performance indices. The hold-last configuration reduced the pitch-angle RMS by 8.9%, 11.2%, and 11.4% at 20, 30, and 40 km/h, respectively. The pitch-rate RMS decreased by 5.5%, 5.1%, and 5.7%. However, these improvements were accompanied by increases in the vertical-acceleration RMS of 5.3%, 5.7%, and 1.0%, respectively, while the actual actuator-force RMS increased by 1.6%, 2.2%, and 0.3%.

Table 12. Sensitivity of TF-MPC performance to future front-road prediction assumptions.

Speed [km/h]	Prediction	Vertical Acc. RMS [m/s^2]	Pitch RMS [deg]	Pitch Rate RMS [deg/s]	Actual Force RMS [N]
20	Zero-input	0.2837	0.3060	1.2620	483.8
	Hold-last	0.2987	0.2788	1.1926	491.5
30	Zero-input	0.2908	0.2264	1.2259	459.2
	Hold-last	0.3074	0.2010	1.1630	469.5
40	Zero-input	0.3090	0.1810	1.2000	468.1
	Hold-last	0.3120	0.1603	1.1311	469.7

The results indicate that the treatment of future front-road excitation affects the predicted coupled heave–pitch response and the resulting control–performance trade-offs. Although the hold-last assumption improves pitch-attitude regulation under the investigated bump conditions, these improvements do not establish its general suitability for future road prediction.

In particular, the inverse-TF-based reconstructed road signal may contain estimation errors due to measurement noise or model mismatch. Under the hold-last assumption, any error in the latest estimate is propagated throughout the prediction horizon, potentially distorting the predicted response and resulting control actions. Moreover, retaining the current road elevation for the entire prediction horizon may overestimate the duration of excitation after the front wheel leaves the bump. These potential effects were not independently quantified in the present comparison.

Accordingly, the original zero-input assumption was retained to avoid introducing an unvalidated extrapolation of reconstructed-road information. Although this assumption can underestimate continuing front-road excitation, it provides a simple causal prediction formulation without relying on the persistence of uncertain estimates. The present results are therefore interpreted as a sensitivity analysis rather than evidence that either assumption provides universally superior prediction accuracy or robustness.

4.4.8. Sensitivity to Effective Preview Delay

To distinguish the influence of effective preview delay from changes in temporal road excitation associated with vehicle speed, an additional sensitivity analysis was conducted at a fixed speed of 30 km/h using the nominal 0.10 m high, 3.6 m long bump. The LQSOF gains, road-reconstruction method, MPC weighting coefficients, actuator model, force constraints, and fixed prediction and control horizons of 150 steps were maintained unchanged.

The effective-delay parameter was varied from 22 to 62 ms in increments of 10 ms. For the 3.01 m wheelbase, the corresponding usable preview interval decreased from approximately 0.339 to 0.299 s. In the implemented preview-buffer formulation, changing the effective delay modifies both the available preview interval and the temporal reference positions of the reconstructed road samples, while the physical road excitation remains unchanged.

Table 13 summarizes the corresponding suspension-performance indices. As the effective delay increased from 22 to 62 ms, the pitch-angle RMS increased from 0.2264° to 0.2346° (3.62%), while the pitch-rate RMS increased from 1.2259°/s to 1.2465°/s (1.68%). In contrast, the vertical-acceleration RMS decreased slightly from 0.2908 to 0.2902 m/s^2 (0.21%), and the actual actuator-force RMS decreased from 459.2 to 457.3 N (0.41%).

Table 13. Sensitivity of TF-MPC performance to the effective preview delay at 30 km/h.

Effective Delay [ms]	Available Preview [s]	Vertical Acc. RMS [m/s^2]	Pitch RMS [deg]	Pitch Rate RMS [deg/s]	Actual Force RMS [N]
22	0.339	0.2908	0.2264	1.2259	459.2
32	0.329	0.2908	0.2292	1.2334	458.6
42	0.319	0.2905	0.2315	1.2392	458.1
52	0.309	0.2903	0.2333	1.2437	457.7
62	0.299	0.2902	0.2346	1.2465	457.3

The intermediate delay conditions exhibited consistent trends, with gradually increasing pitch-angle and pitch-rate RMS values. These results indicate that the effective-delay setting influences the balance between vertical-response suppression and pitch-attitude regulation. Pitch regulation exhibited greater sensitivity, whereas vertical-acceleration and actuator-force RMS remained comparatively insensitive over the investigated range.

Because vehicle speed and road geometry were fixed, these changes are not attributable to variations in the temporal excitation associated with the speed sweep. However, the present analysis characterizes the implemented effective-delay parameter under the investigated localized-bump condition and does not establish general robustness to physical sensor latency or road-reconstruction errors.

5. Conclusions

This study developed a reconstructed-road wheelbase-preview MPC framework for an existing LQSOF-controlled active suspension. The additional rear command is optimized using predictions of future baseline feedback action and actuator-force dynamics, without requiring a forward-looking road sensor. The complete configuration improved the pitch-angle and pitch-rate RMS relative to LQSOF under the investigated 20–40 km/h bump conditions, while vertical-response and actuator-demand trade-offs remained.

The front-compensation-only comparison identified additional pitch-angle RMS reductions of 16.0% and 11.8% when rear MPC was enabled at 20 and 30 km/h. TF-MPC also achieved a lower pitch-angle RMS than every tested proportional rear-gain case at these speeds, although nominal TF Preview provided lower vertical-acceleration and pitch-

rate RMS values. At 40 km/h, front compensation alone and proportional compensation with a rear-gain factor of 1.5 produced lower body-response RMS values than TF-MPC. The latter proportional case required a greater actual actuator-force RMS. These results establish condition-specific pitch-angle benefits and actuator-effort trade-offs rather than uniform superiority over proportional compensation.

The controlled prediction-model ablation and sensitivity studies characterize the roles of feedback prediction, actuator dynamics, and disturbance conditions. Actuator-model mismatch and road-reconstruction sensitivity to measurement noise and sprung-mass variations were assessed separately. The demonstrated control benefits remain specific to the investigated localized-bump conditions. Further investigation of reconstruction reliability, constraint-feasibility management, and fallback control is required before extending the verified operating range. Future research will also consider occupant-oriented ride performance using ISO 2631-1 frequency-weighted acceleration and vibration dose metrics, together with broader output-weight optimization, to explore further improvements in vertical-response suppression and pitch-attitude regulation. Broadband ISO 8608 [34] road-class performance, asymmetric heave–pitch–roll operation, and experimental complete-loop real-time validation remain additional directions for future work.

Author Contributions: Conceptualization, Y.J.; methodology, S.J. and Y.J.; software, S.J.; validation, S.J.; formal analysis, S.J. and Y.J.; investigation, S.J.; data curation, S.J.; visualization, S.J.; writing—original draft preparation, S.J. and Y.J.; writing—review and editing, Y.J.; supervision, Y.J.; project administration, Y.J. All authors have read and agreed to the published version of the manuscript.

Funding: This work was supported by the Technology Innovation Program (RS-2024-00450380, Development of Driving System Technology for Export-Type Multi-Purpose Urban Railway Vehicles) funded by the Ministry of Trade, Industry and Energy (MOTIE, Korea).

Data Availability Statement: The data supporting the findings of this study are available from the corresponding author upon reasonable request. The CarSim vehicle model and commercial software components are subject to third-party licensing restrictions and are therefore not publicly redistributed.

Acknowledgments: During the preparation of this manuscript, the authors used ChatGPT (OpenAI, GPT-5.6 Sol) for language editing, refinement of manuscript organization, and improvement of the presentation of explanatory text and mathematical formulations. The tool did not independently perform simulations, generate research data, conduct numerical analyses, or determine scientific conclusions. All technical content, interpretations, and conclusions were reviewed and verified by the authors, who take full responsibility for the content of this publication.

Conflicts of Interest: The authors declare no conflicts of interest.

Abbreviations

The following abbreviations are used in this manuscript:

LQ	Linear–Quadratic
LQSOF	Linear–Quadratic Static Output Feedback
MPC	Model Predictive Control
P2P	Peak-to-Peak
RMS	Root Mean Square
TF	Transfer Function
TF-MPC	Transfer-Function-Reconstruction-Based Wheelbase-Preview MPC

References

1. Yu, M.; Evangelou, S.A.; Dini, D. Advances in active suspension systems for road vehicles. *Engineering* **2024**, *33*, 160–177. [CrossRef]

2. Theunissen, J.; Tota, A.; Gruber, P.; Dhaens, M.; Sorniotti, A. Preview-based techniques for vehicle suspension control: A state-of-the-art review. *Annu. Rev. Control* **2021**, *51*, 206–235. [CrossRef]
3. Theunissen, J.; Sorniotti, A.; Gruber, P.; Fallah, S.; Ricco, M.; Kvasnica, M.; Dhaens, M. Regionless explicit model predictive control of active suspension systems with preview. *IEEE Trans. Ind. Electron.* **2020**, *67*, 4877–4888. [CrossRef]
4. Song, S.; Wang, J. Incremental model predictive control of active suspensions with estimated road preview information from a lead vehicle. *J. Dyn. Syst. Meas. Control* **2020**, *142*, 121004. [CrossRef]
5. Papadimitrakis, M.; Alexandridis, A. Active vehicle suspension control using road preview model predictive control and radial basis function networks. *Appl. Soft Comput.* **2022**, *120*, 108646. [CrossRef]
6. Kaldas, M.M.; Soliman, A.M.A.; Abdallah, S.A.; Mohammad, S.S.; Amien, F.F. Road preview control for active suspension system. *SAE Int. J. Veh. Dyn. Stab. NVH* **2022**, *6*, 371–383. [CrossRef]
7. Huang, T.; Wang, J.; Pan, H. Adaptive bioinspired preview suspension control with constrained velocity planning for autonomous vehicles. *IEEE Trans. Intell. Veh.* **2023**, *8*, 3925–3935. [CrossRef]
8. Kim, J.; Lee, T.; Kim, C.-J.; Yi, K. Model predictive control of a semi-active suspension with a shift delay compensation using preview road information. *Control Eng. Pract.* **2023**, *137*, 105584. [CrossRef]
9. Li, Q.; Chen, Z.; Song, H.; Dong, Y. Model predictive control for speed-dependent active suspension system with road preview information. *Sensors* **2024**, *24*, 2255. [CrossRef]
10. Liu, Z.; Si, Y.; Sun, W. Ride comfort oriented integrated design of preview active suspension control and longitudinal velocity planning. *Mech. Syst. Signal Process.* **2024**, *208*, 110992. [CrossRef]
11. Mazouchi, M.; Li, Z.; Srivastava, V.; Tai, W.-C.; Goryca, J. Learning-enhanced active vehicle suspension control using preview-augmented model predictive control and Gaussian process. *IFAC-PapersOnLine* **2024**, *58*, 246–251. [CrossRef]
12. Yu, S.; Guo, J.; Xu, M.; Zhang, S.; Zhuang, Y.; Lin, B. Road preview MPC of semi-active suspension with magneto-rheological damper. *Int. J. Robust Nonlinear Control* **2025**, *35*, 2736–2759. [CrossRef]
13. Bai, M.; Wang, J.; Sun, W. Coupled control of preview active suspension and longitudinal dynamics for autonomous vehicle. *IEEE Trans. Syst. Man Cybern. Syst.* **2025**, *55*, 4656–4669. [CrossRef]
14. Bai, M.; Sun, W. Disturbance-resilient model predictive control for active suspension systems with perception errors in road preview information. *J. Frankl. Inst.* **2025**, *362*, 107957. [CrossRef]
15. Yim, S. Preview control with virtual disturbance for active suspension systems. *Appl. Sci.* **2025**, *15*, 12743. [CrossRef]
16. Seok, J.; Jo, J.; Kim, Y.; Kim, H.; Jung, I.; Jeong, M.; Kim, N.; Jo, K. LiDAR-based road height profile estimation and bump detection for preview suspension. *IEEE Trans. Intell. Veh.* **2025**, *10*, 4679–4694. [CrossRef]
17. Liu, W.; Wang, R.; Ding, R.; Meng, X.; Yang, L. On-line estimation of road profile in semi-active suspension based on unsprung mass acceleration. *Mech. Syst. Signal Process.* **2020**, *135*, 106370. [CrossRef]
18. Kim, G.W.; Kang, S.W.; Kim, J.S.; Oh, J.S. Simultaneous estimation of state and unknown road roughness input for vehicle suspension control system based on discrete Kalman filter. *Proc. Inst. Mech. Eng. Part D J. Automob. Eng.* **2020**, *234*, 1610–1622. [CrossRef]
19. Ding, R.; Wang, R.; Meng, X.; Liu, W.; Chen, L. Intelligent switching control of hybrid electromagnetic active suspension based on road identification. *Mech. Syst. Signal Process.* **2021**, *152*, 107355. [CrossRef]
20. Wang, R.; Liu, W.; Ding, R.; Meng, X.; Sun, Z.; Yang, L.; Sun, D. Switching control of semi-active suspension based on road profile estimation. *Veh. Syst. Dyn.* **2022**, *60*, 1972–1992. [CrossRef]
21. Pham, T.-P. Generalized H_2 observer for road profile estimation in the automotive suspension system. *Heliyon* **2024**, *10*, e39928. [CrossRef]
22. Modi, H.; Hajidavalloo, M.R.; Li, Z.; Zheng, M. Robust iterative learning for collaborative road profile estimation and active suspension control in connected vehicles. *IFAC-PapersOnLine* **2024**, *58*, 234–239. [CrossRef]
23. Kwon, B.; Kang, D.; Yi, K. Wheelbase preview control of an active suspension with a disturbance-decoupled observer to improve vehicle ride comfort. *Proc. Inst. Mech. Eng. Part D J. Automob. Eng.* **2020**, *234*, 1725–1745. [CrossRef]
24. Li, W.; Xie, Z.; Zhao, J.; Wong, P.K.; Wang, H.; Wang, X. Static-output-feedback based robust fuzzy wheelbase preview control for uncertain active suspensions with time delay and finite frequency constraint. *IEEE/CAA J. Autom. Sin.* **2021**, *8*, 664–678. [CrossRef]
25. Zhao, J.; Wang, X.; Wong, P.K.; Xie, Z.; Jia, J.; Li, W. Multi-objective frequency domain-constrained static output feedback control for delayed active suspension systems with wheelbase preview information. *Nonlinear Dyn.* **2021**, *103*, 1757–1774. [CrossRef]
26. Wang, J.; Yang, C.; Liu, S.; Zhang, L.; Fang, J. Vehicle posture wheelbase preview control of in-wheel motors drive intelligent vehicle on potholed road. *Proc. Inst. Mech. Eng. Part D J. Automob. Eng.* **2025**, *239*, 5494–5506. [CrossRef]
27. Yang, L.; Chen, H.; Liu, L.; Wang, Q.; Zhang, Z.; Tan, K. Wheelbase-preview predictive controller for active suspension incorporating road profile estimation. *J. Low Freq. Noise Vib. Act. Control* **2026**, *45*, 1582–1602. [CrossRef]
28. Ma, K.; Shao, S.; Zhang, T.; Lu, L.; Li, L.; Ren, C. A time-varying delay control method based on equivalent frequency band for preview suspension systems. *Eur. J. Control* **2026**, *87*, 101445. [CrossRef]

29. Tu, D.T.; Giang, N.T.; Linh, N.H. Optimal vibration control of half-car suspension system integrated with human biodynamic model using Gray Wolf Optimizer. *Proc. Inst. Mech. Eng. Part D J. Automob. Eng.* **2026**, *onlinefirst*. [CrossRef]
30. Do, T.T. Comprehensive performance and robustness analysis of an active half-vehicle suspension with roll dynamics using an enhanced static output-feedback H∞ control framework. *Proc. Inst. Mech. Eng. Part D J. Automob. Eng.* **2026**, *onlinefirst*. [CrossRef]
31. Lio, W.H.; Rossiter, J.A.; Jones, B.L. Modular Model Predictive Control upon an Existing Controller. *Processes* **2020**, *8*, 855. [CrossRef]
32. Mayne, D.Q.; Rawlings, J.B.; Rao, C.V.; Scokaert, P.O.M. Constrained Model Predictive Control: Stability and Optimality. *Automatica* **2000**, *36*, 789–814. [CrossRef]
33. *ISO 2631-1:1997*; Mechanical Vibration and Shock—Evaluation of Human Exposure to Whole-Body Vibration—Part 1: General Requirements. International Organization for Standardization: Geneva, Switzerland, 1997.
34. *ISO 8608:2016*; Mechanical Vibration—Road Surface Profiles—Reporting of Measured Data. International Organization for Standardization: Geneva, Switzerland, 2016.

Disclaimer/Publisher's Note: The statements, opinions and data contained in all publications are solely those of the individual author(s) and contributor(s) and not of MDPI and/or the editor(s). MDPI and/or the editor(s) disclaim responsibility for any injury to people or property resulting from any ideas, methods, instructions or products referred to in the content.